

Long-lived and transient supersolid behaviors in dipolar quantum gases

L. Chomaz,¹ D. Petter,¹ P. Ilzhöfer,² G. Natale,¹ A. Trautmann,² C. Politi,² G. Durastante,^{1,2}
R. M. W. van Bijnen,² A. Patscheider,¹ M. Sohmen,^{1,2} M. J. Mark,^{1,2} and F. Ferlaino^{1,2,*}

¹*Institut für Experimentalphysik, Universität Innsbruck,
Technikerstraße 25, 6020 Innsbruck, Austria*

²*Institut für Quantenoptik und Quanteninformation,
Österreichische Akademie der Wissenschaften,
Technikerstraße 21a, 6020 Innsbruck, Austria*

(Dated: March 12, 2019)

By combining theory and experiments, we demonstrate that dipolar quantum gases of both ¹⁶⁶Er and ¹⁶⁴Dy support a state with supersolid properties, where a spontaneous density modulation and a global phase coherence coexist. This paradoxical state occurs in a well defined parameter range, separating the phases of a regular Bose-Einstein condensate and of an insulating droplet array, and is rooted in the roton mode softening, on the one side, and in the stabilization driven by quantum fluctuations, on the other side. Here, we identify the parameter regime for each of the three phases. In the experiment, we rely on a detailed analysis of the interference patterns resulting from the free expansion of the gas, quantifying both its density modulation and its global phase coherence. Reaching the phases via a slow interaction tuning, starting from a stable condensate, we observe that ¹⁶⁶Er and ¹⁶⁴Dy exhibit a striking difference in the lifetime of the supersolid properties, due to the different atom loss rates in the two systems. Indeed, while in ¹⁶⁶Er the supersolid behavior only survives a few tens of milliseconds, we observe coherent density modulations for more than 150 ms in ¹⁶⁴Dy. Building on this long lifetime, we demonstrate an alternative path to reach the supersolid regime, relying solely on evaporative cooling starting from a thermal gas.

INTRODUCTION

Supersolidity is a paradoxical quantum phase of matter where both crystalline and superfluid order coexist [1–3]. Such a counter-intuitive phase, featuring rather antithetic properties, has been originally considered for quantum crystals with mobile bosonic vacancies, the latter being responsible for the superfluid order. Solid ⁴He has been long considered a prime system to observe such a phenomenon [4, 5]. However, after decades of theoretical and experimental efforts, an unambiguous proof of supersolidity in solid ⁴He is still missing [6, 7].

In search of more favorable and controllable systems, ultracold atoms emerged as a very promising candidate, thanks to their highly tunable interactions. Theoretical works point to the existence of a supersolid ground state in different cold-atom settings, including dipolar [8] and Rydberg particles [9, 10], cold atoms with a soft-core potential [11], or lattice-confined systems [7]. Breakthrough experiments with Bose-Einstein condensates (BECs) coupled to light have recently demonstrated a state with supersolid properties [12, 13]. While in these systems indeed two continuous symmetries are broken, the crystal periodicity is set by the laser wavelength, making the supersolid incompressible.

Another key notion concerns the close relation between a possible transition to a supersolid ground state and the existence of a local energy minimum at large momentum in the excitation spectrum of a non-modulated superfluid, known as roton mode [14]. Since excitations corresponding to a periodic density modulation at the roton

wavelength are energetically favored, the existence of this mode indicates the system’s tendency to crystallize [15] and it is predicted to favor a transition to a supersolid ground state [4, 5, 9].

Remarkably, BECs of highly magnetic atoms, in which the particles interact through the long-range and anisotropic dipole-dipole interaction (DDI), appear to gather several key ingredients for realizing a supersolid phase. First, as predicted more than fifteen years ago [16, 17] and recently demonstrated in experiments [18, 19], the partial attraction in momentum space due to the DDI gives rise to a roton minimum. The corresponding excitation energy, i. e. the roton gap, can be tuned in the experiments down to vanishing values. Here, the excitation spectrum softens at the roton momentum and the system becomes unstable. Second, there is a non-trivial interplay between the trap geometry and the phase diagram of a dipolar BEC. For instance, our recent observations have pointed out the advantage of axially-elongated trap geometries (i. e. cigar-shaped) compared to the typically considered cylindrically-symmetric ones (i. e. pancake-shaped) in enhancing the visibility of the roton excitation in experiments. Last but not least, while the concept of a fully softened mode is typically related to instabilities and disruption of a coherent quantum phase, groundbreaking works in the quantum-gas community have demonstrated that quantum fluctuations can play a crucial role in stabilizing a dipolar BEC [20–26]. Such a stabilization mechanism enables the existence, beyond the mean-field instability, of a variety of stable ground states, from a single macro-droplet

[22, 24, 27] to striped phases [28], and droplet crystals [29]; see also related works [30–33]. For multi-droplet ground states, efforts have been devoted to understand if a phase coherence among ground-state droplets could be established [28, 29]. However, previous experiments with ^{164}Dy have shown the absence of phase coherence across the droplets [28], probably due to the limited atom numbers.

Droplet ground-states, quantum stabilization, and dipolar rotons have raised a huge excitement with very recent advancements adding key pieces of information to the supersolid scenario. The quench experiments in an ^{166}Er BEC at the roton instability have revealed out-of-equilibrium modulated states with an early-time phase coherence over a timescale shorter than a quarter of the oscillation period along the weak-trap axis [18]. In the same work, it has been suggested that the roton softening combined with the quantum stabilization mechanism may open a promising route towards a supersolid ground state. A first confirmation came from a recent theoretical work [34], considering an Er BEC in an infinite elongated trap with periodic boundary conditions and tight transverse confinement. The supersolid phase appears to exist within a narrow region in interaction strength, separating a roton excitation with a vanishing energy and an incoherent assembly of insulating droplets. Almost simultaneously, experiments with ^{162}Dy BECs in a shallow elongated trap, performing a slow tuning of the contact interaction, reported on the production of stripe states with phase coherence persisting up to half of the weak trapping period [35]. More recently, such observations have been confirmed in another ^{162}Dy experiment [36]. Here, theoretical calculations showed the existence of a phase-coherent droplet ground-state, linking the experimental findings to the realization of a state with supersolid properties. The results on ^{162}Dy show however transient supersolid properties whose lifetime is limited by fast inelastic losses caused by three-body collisions [35, 36]. These realizations raise the crucial question of whether a long-lived or stationary supersolid state can be created despite the usually non-negligible atom losses and the crossing of a discontinuous phase transition, which inherently creates excitations in the system.

In this work, we study both experimentally and theoretically the phase diagram of degenerate gases of highly magnetic atoms beyond the roton softening. Our investigations are carried out using two different experimental setups producing BECs of ^{166}Er [22, 37] and of ^{164}Dy [38], and rely on a fine tuning of the contact-interaction strength in both systems. In the regime of interest, these two atomic species have different contact-interaction scattering lengths, a_s , whose precise dependence on the magnetic field is known only for Er [18, 22, 39], and different three-body-loss rate coefficients. Moreover, Er and Dy possess different magnetic moments, μ , and masses, m , yielding the dipolar lengths, $a_{\text{dd}} = \mu_0 \mu^2 m / 12\pi \hbar^2$,

of $65.5 a_0$ and $131 a_0$, respectively. Here μ_0 is the vacuum permeability, $\hbar = h/2\pi$ the reduced Planck constant, and a_0 the Bohr radius. For both systems, we find states showing hallmarks of supersolidity, namely the coexistence of density modulation and global phase coherence. For such states, we quantify the extent of the a_s -parameter range for their existence and study their lifetime. For ^{166}Er , we find results very similar to the one recently reported for ^{162}Dy [35, 36], both systems being limited by strong three-body losses, which destroy the supersolid properties in about half of a trap period. However, for ^{164}Dy , we have identified an advantageous magnetic-field region where losses are very low and large BECs can be created. In this condition, we observe that the supersolid properties persist over a remarkably long time, well exceeding the trap period. Based on such a high stability, we finally demonstrate a novel route to reach the supersolid state, based on evaporative cooling from a thermal gas.

THEORETICAL DESCRIPTION

As a first step in our study of the supersolid phase in dipolar BECs, we compute the ground-state phase diagram for both ^{166}Er and ^{164}Dy quantum gases. The gases are confined in a cigar-shaped harmonic trap, as illustrated in Fig. 1(a). Our theory is based on numerical calculations of the extended Gross-Pitaevskii equation (eGPE) [40], which includes our anisotropic trapping potential, the short-range contact and long-range dipolar interactions at a mean-field level, as well as the first-order beyond-mean-field correction in the form of a Lee-Huang-Yang (LHY) term [18, 22–24, 27]. We note that, while both the exact strength of the LHY term and its dependence on the gas characteristics are under debate [18, 19, 25, 31, 41], the importance of such a term, scaling with a higher power in density, is essential for stabilizing states beyond the mean-field instability [18, 25, 41]; see also [8, 42–44].

Our theoretical results are summarized in Fig. 1. By varying the condensed-atom number, N , and a_s , the phase diagram shows three very distinct phases. To illustrate them, we first describe the evolution of the integrated in-situ density profile $n(y)$ with fixed N for varying a_s , Fig. 1(b). The first phase, appearing at large a_s , resembles a regular dilute BEC. It corresponds to a non-modulated density profile of low peak density and large axial size, σ_y , exceeding several times the corresponding harmonic oscillator length ($\ell_y = \sqrt{\hbar/m\omega_y}$), see Fig. 1(e) and the region denoted BEC in (f) and (g). The second phase appears when decreasing a_s down to a certain critical value, a_s^* . Here, the system undergoes an abrupt transition to a periodic density-modulated ground state, consisting of an array of overlapping narrow droplets, each of high peak density. Because the droplets are coupled

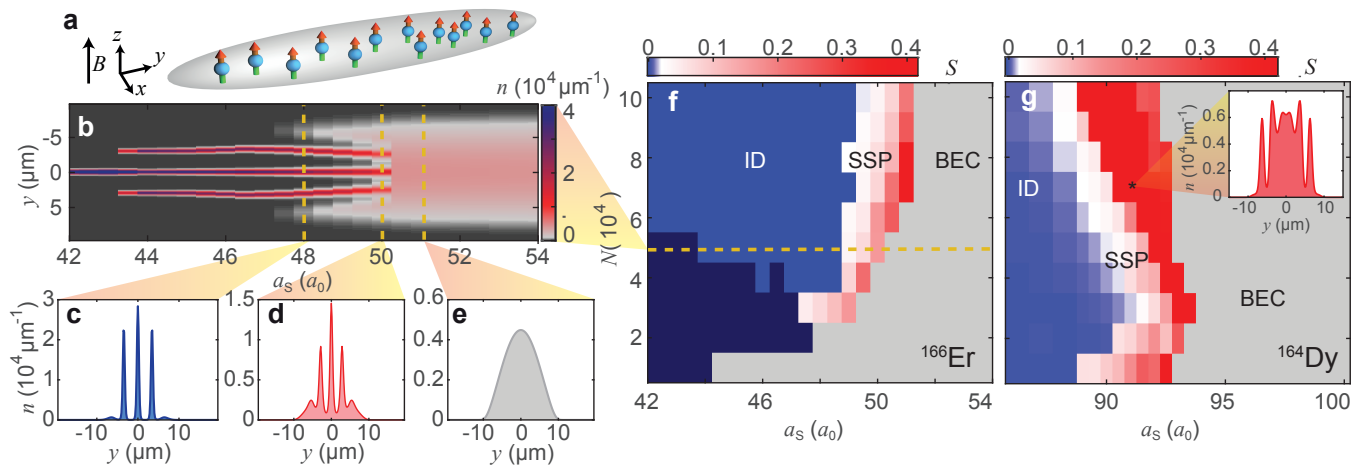


FIG. 1. **Phase diagram of an ^{166}Er and a ^{164}Dy dipolar BEC in a cigar-shaped trap.** (a) Illustration of the trap geometry with atomic dipoles oriented along z . (b) Integrated density profile as a function of a_s for an ^{166}Er ground state of $N = 5 \times 10^4$. In the colorbar, the density scale is upper-limited to $4 \times 10^4 \mu\text{m}^{-1}$ in order to enhance the visibility in the supersolid regime. (c–e) Exemplary density profiles for an insulating-droplet state (ID) at $a_s = 48 a_0$, for a state with supersolid properties (SSP) at $50 a_0$, and for a BEC at $51 a_0$, respectively. (f, g) Phase diagrams for ^{166}Er and ^{164}Dy for trap frequencies $\omega_{x,y,z} = 2\pi \times (145, 31.5, 151)$ Hz and $2\pi \times (225, 37, 135)$ Hz, respectively. The gray color identifies ground states with a single peak in $n(y)$ of large Gaussian width, $\sigma_y > 2\ell_y$. The dark blue region in (f) shows the region where $n(y)$ exhibits a single sharp peak, $\sigma_y \leq 2\ell_y$ and no density modulation. The red-to-blue colormap shows S in the case of a density modulated $n(y)$. In (g) the colormap is upper-limited to 0.42 to enhance visibility in the low N regime. The inset in (g) shows the calculated density profile for ^{164}Dy at $N = 7 \times 10^4$ and $a_s = 91 a_0$.

to each other via a density overlap, later quantified in terms of the link strength S , particles can tunnel from one droplet to a neighboring one, establishing a global phase coherence across the cloud; see Fig. 1(d). Such a phase, in which periodic density modulation and phase coherence coexist, is identified as the supersolid one [10, 34]; SSP region in (f) and (g). When further decreasing a_s , we observe a fast reduction of the density overlap, which eventually vanishes; see Fig. 1(c). Here, the droplets become fully separated. Under realistic experimental conditions, it is expected that the phase relation between such droplets cannot be maintained; see later discussion. We identify this third phase as the one of an insulating droplet array [27, 28, 45]; ID region in (f) and (g). The number of droplets in the array decreases with lowering either a_s (see (b)) or N , eventually resulting in a single droplet of high peak density, as in Refs. [24, 27]; see dark blue region in (f). The existence of these three phases (BEC-SSP-ID) is consistent with recent calculations considering an infinitely elongated Er BEC [34] and a cigar-shaped ^{162}Dy BEC [36], illustrating the generality of this behavior in dipolar gases.

To study the supersolid character of the density-modulated phases, we compute the average of the wavefunction overlap between neighboring droplets, S . As an ansatz to extract S , we use a Gaussian function to describe the wavefunction of each individual droplet. This is found to be an appropriate description from an analysis of the density profiles of Fig. 1(b-d); see also [46]. For two droplets at a distance d and of identical Gaus-

sian widths, σ_y , along the array direction, S is simply $S = \exp(-d^2/4\sigma_y^2)$. Here, we generalize the computation of the wavefunction overlap to account for the difference in widths and amplitudes among neighboring droplets. This analysis allows to distinguish between the two types of modulated ground states, SSP and ID in Fig. 1(f-g). Within the Josephson-junction picture [47–49], the tunneling rate of atoms between neighboring droplets depends on the wavefunction overlap, and an estimate for the single-particle tunneling rate can be derived within the Gaussian approximation [46]; see also [40]. The ID phase corresponds to vanishingly small values of S , yielding tunneling times extremely long compared to any other relevant time scale. In contrast, the supersolid phase is identified by a substantial value of S , with a correspondingly short tunneling time.

As shown in Fig. 1(f-g), a comparative analysis of the phase diagram for ^{166}Er and ^{164}Dy reveals similarities between the two species (see also Ref. [36]). A supersolid phase is found for sufficiently high N , in a narrow region of a_s , upper-bounded by the critical value $a_s^*(N)$. For intermediate N , a_s^* increases with increasing N . We note that, for low N , the non-modulated BEC evolves directly into a single droplet state for decreasing a_s [50]. In this case, no supersolid phase is found in between, see also Refs. [24, 27]. Despite the general similarities, we see that the supersolid phase for ^{164}Dy appears for lower atom number than for Er and has a larger extension in a_s . We note that, at large N and for decreasing a_s , Dy exhibits ground states with a density modulation ap-

pearing first in the wings, which then progresses inwards until a substantial modulation over the whole cloud is established [51]; see inset (g). In this regime, we also observe that a_s^* decreases with increasing N . These type of states have not been previously reported and, although challenging to access in experiments because of the large N , they deserve further theoretical investigations.

EXPERIMENTAL SEQUENCE FOR $^{166}\text{ERBIUM}$ AND $^{164}\text{DYSPROSIUM}$

To experimentally access the above-discussed physics, we produce dipolar BECs of either ^{166}Er or ^{164}Dy atoms. These two systems are created in different setups and below we summarize the main experimental steps; see also [40].

Erbium – We prepare a stable ^{166}Er BEC following the scheme of Ref. [18]. At the end of the preparation, the Er BEC contains about $N = 8 \times 10^4$ atoms at $a_s = 64.5 a_0$. The sample is confined in a cigar-shaped optical dipole trap with harmonic frequencies $\omega_{x,y,z} = 2\pi \times (145, 31.5, 151)$ Hz. A homogeneous magnetic field, B , polarizes the sample along z and controls the value of a_s via a magnetic Feshbach resonance (FR) [18, 22, 40]. Our measurements start by linearly ramping down a_s within 20 ms and waiting additional 15 ms so that a_s reaches its target value [40]. We note that ramping times between 20 and 60 ms have been tested in the experiment and we do not record a significant difference in the system’s behavior. After the 15 ms stabilization time, we then hold the sample for a variable time t_h before switching off the trap. Finally, we let the cloud expand for 30 ms and perform absorption imaging along the z (vertical) direction, from which we extract the density distribution of the cloud in momentum space, $n(k_x, k_y)$.

Dysprosium – The experimental procedure to create a ^{164}Dy BEC follows the one described in Ref. [38]; see also [40]. Similarly to Er, the Dy BEC is also confined in a cigar-shaped optical dipole trap and a homogeneous magnetic field B sets the quantization axis along z and the value of a_s . For Dy, we will discuss our results in terms of magnetic field, B , since the a_s -to- B conversion is not well known in the magnetic-field range considered [25, 40, 41, 52]. In a first set of measurements, we first produce a stable BEC of about $N = 3.5 \times 10^4$ condensed atoms at a magnetic field of $B = 2.5$ G and then probe the phase diagram by tuning a_s . Here, before ramping the magnetic field to access the interesting a_s regions, we slowly increase the power of the trapping beams within 200 ms. The final trap frequencies are $\omega_{x,y,z} = 2\pi \times (300, 16, 222)$ Hz. After preparing a stable BEC, we ramp B to the desired value within 20 ms and hold the sample for t_h [40]. In a second set of measurements, we study a completely different approach to

reach the supersolid state. As discussed later, here we first prepare a thermal sample at a B value where supersolid properties are observed and then further cool the sample until a transition to a coherent droplet-array state is reached. In both cases, at the end of the experimental sequence, we perform absorption imaging after typically 27 ms of time-of-flight (TOF) expansion. The imaging beam propagates horizontally under an angle α of $\approx 45^\circ$ with respect to the weak axis of the trap (y). From the TOF images, we thus extract $n(k_y, k_z)$ with $k_y = \cos(\alpha)k_y + \sin(\alpha)k_x$.

A special property of ^{164}Dy is that its background scattering length is smaller than a_{dd} . This allows to enter the supersolid regime without the need of setting B close to a FR, as done for ^{166}Er and ^{162}Dy , which typically causes severe atom losses due to increased three-body loss coefficients. In contrast, in the case of ^{164}Dy , the supersolid regime is reached by ramping B away from the FR pole used to produce the stable BEC via evaporative cooling, as the a_s -range of Fig. 1(g) lies close to the background a_s reported in Ref. [52]; see also [40]. At the background level, three-body loss coefficients below $1.3 \times 10^{-41} \text{m}^6 \text{s}^{-1}$ have been reported for ^{164}Dy [25].

DENSITY MODULATION AND PHASE COHERENCE

The coexistence of density modulation and phase coherence is the key feature that characterizes the supersolid phase and allows to discriminate it from the BEC and ID cases. To experimentally probe this aspect in our dipolar quantum gases, we record their density distribution after a TOF expansion for various values of a_s across the phase diagram. As for a BEC in a weak optical lattice [53] or for an array of BECs [54–56], the appearance of interference patterns in the TOF images is associated with a density modulation of the in-situ atomic distribution. Moreover, the shot-to-shot reproducibility of the patterns (in amplitude and position) and the persistence of fringes in averaged pictures, obtained from many repeated images taken under the same experimental conditions, reveals the presence of phase coherence across the sample [56].

Figure 2 exemplifies snapshots of the TOF distributions for Er, measured at three different a_s values; see (a-c). Even if very close in scattering length, the recorded $n(k_x, k_y)$ shows a dramatic change in behavior. For $a_s = 54.7(2) a_0$, we observe a non-modulated distribution with a density profile characteristic of a dilute BEC. When lowering a_s to $53.8(2) a_0$, we observe the appearance of an interference pattern in the density distribution, consisting of a high central peak and two almost symmetric low-density side peaks [57]. Remarkably, the observed pattern is very reproducible with a high shot-to-shot stability, as shown in the repeated single snapshots

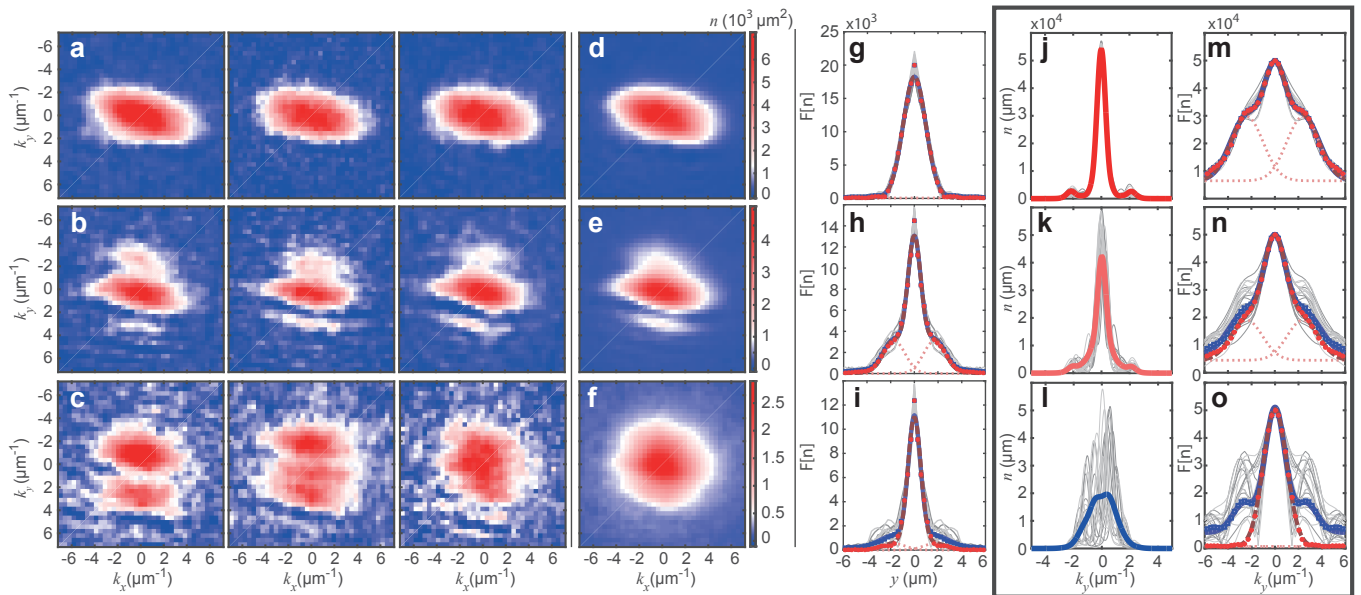


FIG. 2. **Coherence in the interference patterns: measurement and toy model.** (a,b,c) Examples of single TOF absorption images at $t_h = 5$ ms for ^{166}Er at $a_s = \{54.7(2), 53.8(2), 53.3(2)\} a_0$, respectively. Corresponding average pictures for 100 images obtained under the same experimental conditions (d, e, f) and their FT profiles (g, h, i). The grey lines show the FT norm $|\mathcal{F}[n](y)|$ of the individual profiles. The averages, n_M (blue squares) and n_Φ (red dots), are fitted to three-Gaussian functions (blue solid line and brown dashed line, respectively). The dotted lines show the components of the total fitted function corresponding to the two side peaks in n_Φ . (j-l) Interference patterns from the toy-model realizations with 100 independent draws using $N_D = 4$, $d = 2.8 \mu\text{m}$, $\sigma_y = 0.56 \mu\text{m}$ (see text) and for different ϕ_i distributions: (j) $\phi_i = 0$, (k) ϕ_i normally distributed around 0 with 0.2π standard deviation, (l) ϕ_i uniformly distributed between 0 and 2π . (m-o) Corresponding FT profiles for the toy model, same color code as (g-i).

and in the average image (b and e). This behavior indicates a coexistence of density modulation and global phase coherence in the in-situ state, as expected in the supersolid phase. This observation is consistent with our previous quench experiments [18] and with the recent ^{162}Dy experiments [35, 36]. When further lowering a_s to $53.3(2) a_0$, complicated patterns develop with fringes varying from shot-to-shot in number, position, and amplitude, signaling the persistence of in-situ density modulation. However, the interference pattern is completely washed out in the averaged density profiles (f), pointing to the absence of a global phase coherence. We identify this behavior as the one of ID states.

Toy Model – To get an intuitive understanding of the interplay between density modulation and phase coherence and to estimate the role of the different sources of fluctuations in our experiment, we here develop a simple toy model, which is inspired by Ref. [56]; see also Ref. [40]. In our model, the initial state is an array of N_D droplets containing in total N atoms. Each droplet is described by a one-dimensional Gaussian wavefunction, $\psi_i(y)$, of amplitude α_i , phase ϕ_i , width σ_i , and center y_i . To account for fluctuations in the experiments, we allow α_i , $d_i = y_i - y_{i-1}$, and σ_i to vary by 10% around their expectation values. The spread of the phases ϕ_i among the droplets is treated specially as it controls the

global phase coherence of the array. By fixing $\phi_i = 0$ for each droplet or by setting a random distribution of ϕ_i , we range from full phase coherence to the incoherent cases. Therefore, the degree of phase incoherence can be varied by changing the standard deviation of the distribution of ϕ_i .

To mimic our experiment, we compute the free evolution of each individual ψ_i over 30 ms, and then compute the axial distribution $n(y, t) = |\sum_i \psi_i(y, t)|^2$, from which we extract the momentum distribution $n(k_y)$, also accounting for the finite imaging resolution [40]. For each computation run, we randomly draw N_D values for ϕ_i , as well as of σ_i , d_i and α_i and extract $n(k_y)$. We then collect a set of $n(k_y)$ by drawing these values multiple times using the same statistical parameters and compute the expectation value, $\langle n(k_y) \rangle$; see Fig. 2(j-l). The angled brackets denote the ensemble average.

The results of our toy model show large similarity with the observed behavior in the experiment. In particular, while for each single realization one can clearly distinguish multi-peak structures regardless of the degree of phase coherence between the droplets, the visibility of the interference pattern in the averaged $n(k_y)$ survives only if the standard deviation of the phase fluctuations between droplets is small (roughly, below 0.3π). In the incoherent case, we note that the shape of the patterns strongly

vary from shot to shot. Interestingly, the toy model also shows that the visibility of the coherent peaks in the average images is robust against the typical shot-to-shot fluctuations in droplet size, amplitude and distance that occur in the experiments; see (j,k).

Probing density modulation and phase coherence – To separate and quantify the information on the in-situ density modulation and its phase coherence, we analyse the measured interference patterns in Fourier space [36, 58–60]. Here, we extract two distinct averaged density profiles, $n_{\mathcal{M}}$ and n_{Φ} . Their structures at finite y -spatial frequency (i.e. in Fourier space) quantify the two above-mentioned properties.

More precisely, we perform a Fourier transform (FT) of the integrated momentum distributions, $n(k_y)$, denoted $\mathcal{F}[n](y)$. Generally speaking, modulations in $n(k_y)$ induce peaks at finite spatial frequency, $y = y^*$, in the FT norm, $|\mathcal{F}[n](y)|$; see Fig. 2(g-i) and (m-o). Following the above discussion (see also Refs. [56, 61]), such peaks in an individual realization hence reveal a density modulation of the corresponding in-situ state, with a wavelength roughly equal to y^* . Consequently, we consider the average of the FT norm of the individual images, $n_{\mathcal{M}}(y) = \langle |\mathcal{F}[n](y)| \rangle$ as the first profile of interest. The peaks of $n_{\mathcal{M}}$ at finite y then indicate the mere existence of an in-situ density modulation of roughly constant spacing within the different realizations. As second profile of interest, we use the FT norm of the average profile $\langle n(k_y) \rangle$, $n_{\Phi}(y) = |\mathcal{F}[\langle n \rangle](y)|$. Connecting to our previous discussion, the peaks of n_{Φ} at finite y point to the persistence of a modulation in the average $\langle n(k_y) \rangle$, which we identified as a hallmark for a global phase coherence within the density modulated state. In particular we point out that a perfect phase coherence, implying identical interference patterns in all the individual realizations, yields $n_{\mathcal{M}} = n_{\Phi}$ and, thus, identical peaks at finite y in both profiles. We note that, by linearity, n_{Φ} , also matches the norm of the average of the full FT of the individual images, i.e. $n_{\Phi}(y) = |\langle \mathcal{F}[n](y) \rangle|$; see also Ref. [40].

Figure 2 (g-i) and (m-o) demonstrates the significance of our FT analysis scheme by applying it to the momentum distributions from the experiment (d-f) and the ones from the toy model (j-l), respectively. As expected, for the BEC case, both $n_{\mathcal{M}}$ and n_{Φ} show a single peak at zero spatial frequency, $y = 0$, characterizing the absence of density modulation (g). In the case of phase-coherent droplets (e), we observe that $n_{\mathcal{M}}$ and n_{Φ} are superimposed and both show two symmetric side peaks at finite y , in addition to a dominant peak at $y = 0$; see (h). In the incoherent droplet case, we find that, while $n_{\mathcal{M}}$ still shows side peaks at finite y , the ones in n_{Φ} wash out from the averaging, (f, i, l, o). For both coherent and incoherent droplet arrays, the toy-model results show behaviors matching the above description, providing a further justification of our FT-analysis scheme; see (j-o). Our toy model additionally proves two interesting features. First,

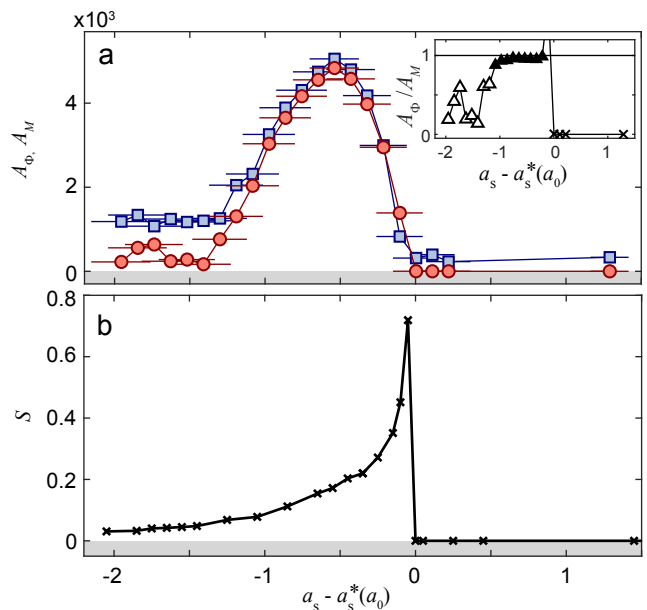


FIG. 3. **Supersolid behavior across the phase diagram.** Measured side-peak amplitudes, A_{Φ} (circles) and $A_{\mathcal{M}}$ (squares) with their ratio in inset (a), and calculated link strength S (b) as a function of $a_s - a_s^*$ for ^{166}Er . For non-modulated states, we set $S = 0$ in theory and $A_{\Phi}/A_{\mathcal{M}} = 0$ in experiment (crosses in inset). In the inset, open and closed symbols correspond to $A_{\Phi}/A_{\mathcal{M}} > 0.8$ and ≤ 0.8 , respectively. In the experiments, we probe the system at a fixed $t_h = 5$ ms. Horizontal error bars are derived from our experimental uncertainty in B , vertical error bars corresponding to the statistical uncertainty from the fit are smaller than the data points. The measured and calculated critical scattering lengths are $a_s^* = 54.9(2) a_0$ and $50.55 a_0$, respectively [62]. The numerical results are obtained for the experimental trap frequencies and for a constant $N = 5 \times 10^4$ [63].

it shows that the equality $n_{\mathcal{M}} = n_{\Phi}$, revealing the global phase coherence of a density modulated state, is remarkably robust to noise in the structure of the droplet arrays; see (j, m). Second, our toy model however shows that phase fluctuations across the droplet array on the order of 0.2π standard deviation are already sufficient to make n_{Φ} and $n_{\mathcal{M}}$ to deviate from each other; see (k, n). The incoherent behavior is also associated with strong variations in the side peak amplitude of the individual realizations of $|\mathcal{F}[n]|$, connecting, e.g. to the observations of Refs. [36].

Finally, to quantify the density modulation and the phase coherence, we fit a three-Gaussian function to both $n_{\mathcal{M}}(y)$ and $n_{\Phi}(y)$ and extract the amplitudes of the finite-spatial-frequency peaks, $A_{\mathcal{M}}$ and A_{Φ} , for both distributions, respectively. Note that for a BEC, which is a phase coherent state, A_{Φ} will be zero since it probes only finite-spatial-frequency peaks; see Fig. 2 (g-i, m-o).

CHARACTERIZATION OF THE SUPERSOLID STATE

We are now in the position to study two key aspects, namely (i) the evolution of the density modulation and phase coherence across the BEC-supersolid-ID phases, and (ii) the lifetime of the coherent density modulated state in the supersolid regime.

Evolution of the supersolid properties across the phase diagram – The first type of investigations is conducted with ^{166}Er since for this species the scattering length and its dependence on the magnetic field has been precisely characterized [18, 22]. After preparing the sample, we ramp a_s to the desired value and study the density patterns as well as their phase coherence by probing the amplitudes A_M and A_Φ as a function of a_s after $t_h = 5$ ms. As shown in Fig. 3(a), in the BEC region (i.e. for large a_s), we observe that both A_M and A_Φ are almost zero, evidencing the expected absence of a density modulation in the system. As soon as a_s reaches a critical value a_s^* , the system's behavior dramatically changes with a sharp and simultaneous increase of both A_M and A_Φ . While the strength of A_M and A_Φ varies with decreasing a_s – first increasing then decreasing – we observe that their ratio A_Φ/A_M remains constant and close to unity over a narrow a_s -range below a_s^* of $\gtrsim 1 a_0$ width; see inset. This behavior pinpoints the coexistence in the system of phase coherence and density modulation, as predicted to occur in the supersolid regime. For $(a_s - a_s^*) < -1 a_0$, we observe that the two amplitudes depart from each other. Here, while the density modulation still survives with A_M saturating to a lower finite value, the global phase coherence is lost with $A_\Phi/A_M < 1$, as expected in the insulating droplet phase.

To get a deeper insight on how our observations compare to the phase-diagram predictions (see Fig. 1), we study the link strength S as a function of a_s ; see Fig. 3(b). Since S quantifies the density overlap between neighboring droplets and is related to the tunneling rate of atoms across the droplet array, it thus provides information on the ability of the system to establish or maintain a global phase coherence. In this plot, we set $S = 0$ in the case where no modulation is found in the ground state. At the BEC-to-supersolid transition, i.e. at $a_s = a_s^*$, a density modulation abruptly appears in the system's ground-state with S taking a finite value. Here, S is maximal, corresponding to a density modulation of minimal amplitude. Below the transition, we observe a progressive decrease of S with lowering a_s , pointing to the gradual reduction of the tunneling rate in the droplet arrays. Close to the transition, we estimate a large tunneling compared to all other relevant timescales. However, we expect this rate to become vanishingly small, on the sub-Hertz level [40], when decreasing a_s 1–2 a_0 below a_s^* . Our observation also hints to the smooth character of the transition from a supersolid to an ID phase, suggesting a

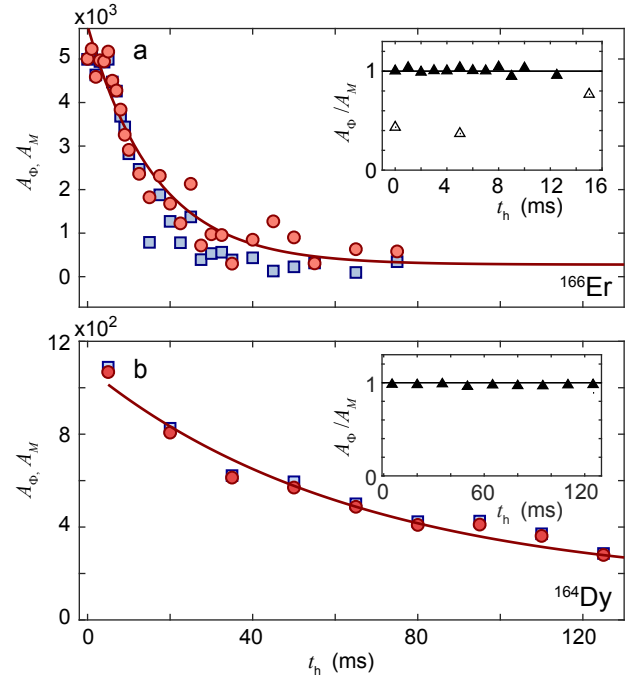


FIG. 4. **Time Evolution of the supersolid properties.** Amplitudes A_Φ (circles) and A_M (squares) in the supersolid regime as a function of the holding time in trap for (a) ^{166}Er at $54.2(2) a_0$, and for (b) ^{164}Dy at 2.04 G. The solid lines are exponential fits to the data. The insets show the time evolution of A_Φ/A_M for the above cases (filled triangles), and, for comparison, in the ID regime (empty triangles) for Er at $a_s = 53.1(2) a_0$ (a).

crossover-type behavior.

The general trend of S , including the extension in a_s where it takes non-vanishing values, is similar to the a_s -behavior of A_M and A_Φ observed in the experiments [62]. We observe in the experiments that the a_s dependence at the BEC-to-supersolid transition appears sharper than at the supersolid-to-ID interface, potentially suggesting a different nature of the two transitions. However, more investigations are needed since atom losses, finite-temperature and finite-size effects can affect, and in particular smoothen, the observed behavior [64–66]. Moreover, dynamical effects, induced by e.g. excitations created at the crossing of the phase transitions or atoms losses during the time evolution, can also play a substantial role in the experimental observations, complicating a direct comparison with the ground state calculations. The time dynamics as well as a different scheme to achieve a state with supersolid properties will be the focus of the remainder of the manuscript.

Lifetime of the supersolid properties – Having identified the a_s range in which our dipolar quantum gas exhibits supersolid properties, the next central question concerns the stability and lifetime of such a fascinating state. Recent experiments on ^{162}Dy have shown the transient character of the supersolid properties, whose lifetime is lim-

ited by three-body losses [35, 36]. In these experiments, the phase coherence is found to survive up to 20 ms after the density modulation has formed. This time corresponds to about half of the weak-trap period. Stability is a key issue in the supersolid regime, especially since the tuning of a_s , used to enter this regime, has a twofold consequence on the inelastic loss rate. First, it gives rise to an increase in the peak density (see Fig. 1b-d) and, second, it may lead to an enhancement of the three-body loss coefficient.

We address this question by conducting comparative studies on ^{166}Er and ^{164}Dy gases. These two species allow us to tackle two substantially different scattering scenarios. Indeed, the background value of a_s for ^{166}Er (as well as for ^{162}Dy) is larger than a_{dd} . Thus, reaching the supersolid regime, which occurs at $a_{\text{dd}}/a_s \approx 1.2 - 1.4$ in our geometry, requires to tune B close to the pole of a FR. This tuning also causes an increase of the three-body loss rate. In contrast, ^{164}Dy realizes the opposite case with the background scattering length smaller than a_{dd} . This feature brings the important advantage of requiring tuning B away from the FR pole to reach the supersolid regime. As we will describe below, this important difference in scattering properties leads to a strikingly longer lifetime of the ^{164}Dy supersolid properties with respect to ^{166}Er and to the recently observed behavior in ^{162}Dy [35, 36].

The measurements proceed as follows. For both ^{166}Er and ^{164}Dy , we first prepare the quantum gas in the stable BEC regime and then ramp a_s to a fixed value in the supersolid regime for which the system exhibits a state of coherent droplets (i. e. $A_\Phi/A_M \approx 1$); see previous discussion. Finally, we record the TOF images after a variable t_h and we extract the time evolution of both A_Φ and A_M . The study of these two amplitudes will allow us to answer the question whether the droplet structure – i. e. the density modulation in space – persists in time whereas the coherence among droplets is lost ($A_M > A_\Phi \rightarrow 0$) or if the density structures themselves vanish in time ($A_M \approx A_\Phi \rightarrow 0$).

As shown in Fig. 4, for both species, we observe that A_Φ and A_M decay almost synchronously with a remarkably longer lifetime for ^{164}Dy (b) than ^{166}Er (a). Interestingly, A_Φ and A_M remain approximately equal during the whole time dynamics; see inset (a-b). This behavior indicates that it is the strength of the density modulation itself and not the phase coherence among droplets that decays over time. Similar results have been found theoretically in Ref. [67]. We connect this decay mainly to three-body losses, especially detrimental for ^{166}Er , and possible excitations created while crossing the BEC-to-supersolid phase transition [40]. For comparison, the inset shows also the behavior in the ID regime for ^{166}Er , where $A_\Phi/A_M < 1$ already at short t_h and remains so during the time evolution [40].

To get a quantitative estimate of the survival time

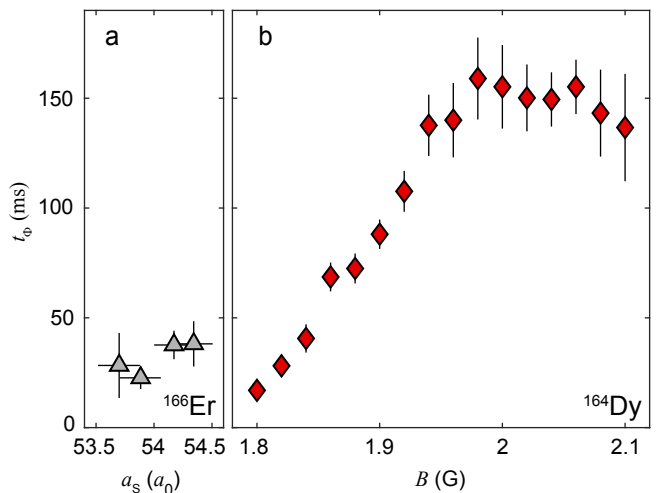


FIG. 5. **Survival time of the coherent density-modulated state.** t_Φ in ^{166}Er as a function of a_s (a) and ^{164}Dy as a function of B (b). The error bars refer to the statistical uncertainty from the fit. The range of investigation corresponds to the supersolid regime for which phase-coherent density-modulated states are observed. This range is particularly narrow for ^{166}Er .

of the phase coherent and density modulated state, we fit a simple exponential function to A_Φ and extract t_Φ , defined as the 1/10 lifetime; see Fig. 4. For ^{166}Er , we extract $t_\Phi = 38(6)$ ms. For $t_h > t_\Phi$, the interference patterns become undetectable in our experiment and we recover a signal similar to the one of a non-modulated BEC state (as in Fig. 2(a,d)). These results are consistent with recent observations of transient supersolid properties in ^{162}Dy [35]. For ^{164}Dy , we observe that the coherent density-modulated state is remarkably long-lived. Here, we find $t_\Phi = 152(13)$ ms.

The striking difference in the lifetime and robustness of the supersolid properties between ^{166}Er and ^{164}Dy becomes even more visible when studying t_Φ as a function of a_s (B for Dy). As shown in Fig. 5, t_Φ for Er remains comparatively low in the investigated supersolid regime and slightly varies between 20 and 40 ms. Similarly to the recent studies with ^{162}Dy , this finding reveals the transient character of the state and opens the question of whether a stationary supersolid state can be reached with these species. On the contrary, for ^{164}Dy we observe that t_Φ first increases with B in the range from 1.8 G to about 1.98 G. Then, for $B > 1.98$ G, t_Φ acquires a remarkably large and almost constant value of about 150 ms over a wide B -range. This shows the long-lived character of the supersolid properties in our ^{164}Dy quantum gas. We note that over the investigated range, a_s is expected to monotonously increase with B [40]. Such a large value of t_Φ exceeds not only the estimated tunneling time across neighbouring droplets but also the weak-axis trap period, which together set the typical timescale to achieve global

equilibrium and to study collective excitations.

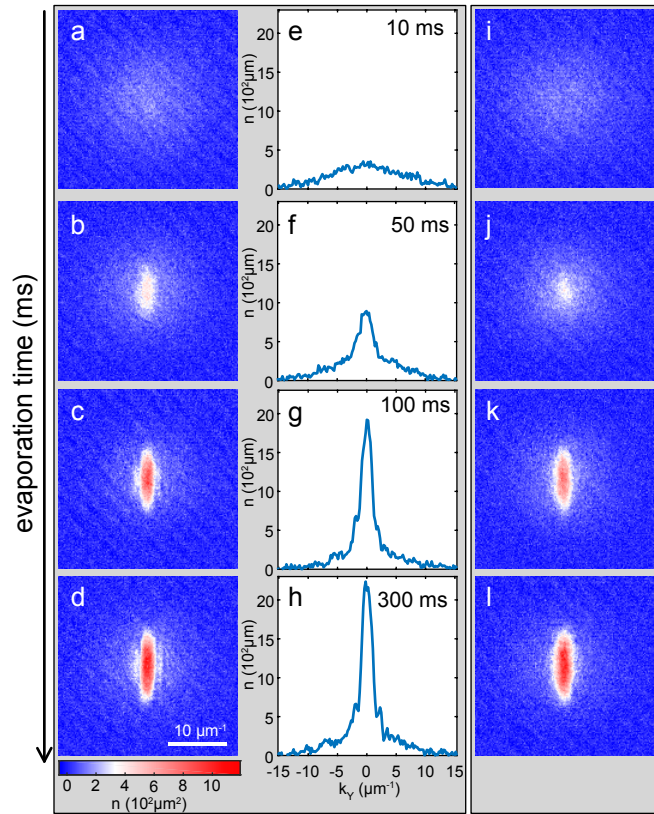


FIG. 6. **Evaporative cooling to a state with supersolid properties.** ^{164}Dy absorption images showing the transition to a state with supersolid properties at 2.43 G (a-d) and to a BEC state at 2.55 G (i-l), via different durations of the last evaporation step. These durations are 10 ms (a,i), 50 ms (b,j), 100 ms (c,k), and 300 ms (d,l). The density profiles (e-h) are integrated over the central regions of the corresponding absorption images (a-d). The colormap indicates the atomic density n in momentum space.

CREATION OF STATES WITH SUPERSOLID PROPERTIES BY EVAPORATIVE COOLING

The long-lived supersolid properties in ^{164}Dy motivate us to explore an alternative route to cross the supersolid phase transition, namely by evaporative cooling instead of interaction tuning. For this set of experiments, we have modified the waists of our trapping beams in order to achieve quantum degeneracy in tighter traps with respect to the one used for condensation in the previous set of measurements. In this way, the interference peaks in the supersolid region are already visible without the need to apply a further compression of the trap since the side-to-central-peak distance in the momentum distribution scales roughly as $1/\ell_z$ [18]. Forced evaporative cooling is performed by reducing the power of the trapping beams piecewise-linearly in subsequent evaporation steps

until a final trap with frequencies $2\pi \times (225, 37, 134)$ Hz is achieved. During the whole evaporation process, which has an overall duration of about 3 s, the magnetic field is kept either at $B = 2.43$ G, where we observe long-lived interference patterns, or at $B = 2.55$ G, where we produce a stable non-modulated BEC. We note that these two B values are very close without any FR lying in between [40].

Figure 6 shows the phase transition from a thermal cloud to a final state with supersolid properties by evaporative cooling. In particular, we study the phase transition by varying the duration of the last evaporation ramp, while maintaining the initial and final trap-beam power fixed. This procedure effectively changes the atom number and temperature in the final trap while keeping the trap parameters unchanged, which is important to not alter the final ground-state phase diagram of the system. At the end of the evaporation, we let the system equilibrate and thermalize for $t_h = 100$ ms, after which we switch off the trap, let the atoms expand for 26.5 ms, and finally perform absorption imaging. We record the TOF images for different ramp durations, i. e. for different thermalization times. For a short ramp, too many atoms are lost such that the critical atom number for condensation is not reached, and the atomic distribution remains thermal; see Fig. 6(a).

By increasing the ramp time, the evaporative cooling becomes more efficient and we observe the appearance of a bimodal density profile with a narrow and dense peak at the center, which we identify as a regular BEC; see Fig. 6(b). By further cooling, the BEC fraction increases and the characteristic pattern of the supersolid state emerges; see Fig. 6(c-d). The observed evaporation process shows a strikingly different behavior in comparison with the corresponding situation at $B = 2.55$ G, where the usual thermal-to-BEC phase transition is observed; see Fig. 6(i-l).

We finally probe the lifetime of the supersolid properties by extracting the time evolution of both the amplitudes A_Φ and A_M , as previously discussed. We use the same experimental sequence as the one in Fig. 6(d) – i. e. 300 ms duration of the last evaporation ramp and 100 ms of equilibration time – and subsequently hold the sample in the trap for a variable t_h . As shown in Fig. 7(a), we observe a very long lifetime with both amplitudes staying large and almost constant over more than 200 ms. At longer holding time, we observe a slow decay of A_Φ and A_M , following the one of the atom number. Moreover, during the dynamics, the ratio A_Φ/A_M stays constant. The long lifetime of the phase-coherent density modulation is also directly visible in the persistence of the interference patterns in the averaged momentum density profiles (similar to Fig. 2(e)), both at intermediate and long times; see Fig. 7(b) and (c), respectively. For even longer t_h , we can not resolve anymore interference patterns in the TOF images. Here, we recover a signal

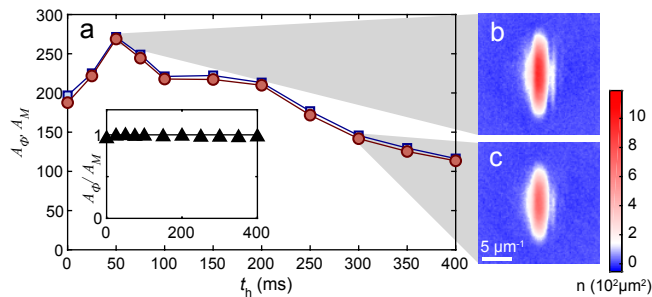


FIG. 7. **Lifetime of the supersolid properties achieved via evaporative cooling.** Time evolution of the amplitudes A_Φ (red circle) and A_M (square) after an evaporation time of 300 ms at 2.43 G and an equilibration time of 100 ms. The inset shows the time evolution of A_Φ/A_M . Averaged absorption images of 25 realizations after 50 ms (b) and 300 ms (c) of holding time. Note that the thermal background has been subtracted from the images. The colormap indicates the atomic density in momentum space.

consistent with a regular BEC of low N .

Achieving the coherent-droplet phase via evaporative cooling is a very powerful alternative path to supersolidity. We speculate that, for instance, excitations, which might be important when crossing the phase transitions by interaction tuning, may be small or removed by evaporation when reaching this state kinematically. Other interesting questions, open to future investigations, are the nature of the phase transition, the critical atom number, and the role of non-condensed atoms.

CONCLUSIONS

For both ^{166}Er and ^{164}Dy dipolar quantum gases, we have identified and studied states showing hallmarks of supersolidity, namely global phase coherence and spontaneous density modulations. These states exist in a narrow scattering-length region, lying between a regular BEC phase and a phase of an insulating droplet array. While for ^{166}Er , similarly to the recently-reported ^{162}Dy case [35, 36], the observed supersolid properties fade out over a comparatively short time because of atom losses, we find that ^{164}Dy exhibits remarkably long-lived supersolid properties. Moreover, we are able to directly create stationary states with supersolid properties by evaporative cooling, demonstrating a powerful alternative approach to interaction tuning on a BEC. This novel technique provides prospects of creating states with supersolid properties while avoiding additional excitations and dynamics. The ability to produce long-lived supersolid states paves the way for future investigations on quantum fluctuations and many-body correlations as well as of collective excitations in such an intriguing many-body quantum state. A central goal of these future investigations lies in proving the superfluid character of this phase,

beyond its global phase coherence [7, 34, 68–70].

Note added– During the course of the present work, we became aware of a related work, reporting a theoretical study of the ground-state phase diagram based on Monte-Carlo calculations [71].

ACKNOWLEDGMENTS

We thank R. Bisset, B. Blakie, M. Boninsegni, G. Modugno, T. Pfau, and in particular L. Santos for many stimulating discussions. Part of the computational results presented have been achieved using the HPC infrastructure LEO of the University of Innsbruck. We acknowledge support by the Austrian Science Fund FWF through the DFG/FWF Forschergruppe (FOR 2247/PI2790), by the ERC Consolidator Grant (RARE, no. 681432), and by a NFRI Grant (MI-RARE, no. ÖAW0600) from the Austrian Academy of Science. G.D. and M.S. acknowledge support by the Austrian Science Fund FWF within the DK-ALM (no. W1259-N27).

* Correspondence and requests for materials should be addressed to Francesca.Ferlaino@uibk.ac.at.

-
- [1] A. F. Andreev and I. M. Lifshitz, *Sov. Phys. JETP* **29**, 1107 (1969).
 - [2] G. V. Chester, *Phys. Rev. A* **2**, 256 (1970).
 - [3] A. J. Leggett, *Phys. Rev. Lett.* **25**, 1543 (1970).
 - [4] D. Kirzhnits and Y. A. Nepomnyashchii, *Sov. Phys. JETP* **32** (1971).
 - [5] T. Schneider and C. P. Enz, *Phys. Rev. Lett.* **27**, 1186 (1971).
 - [6] S. Balibar, *Nature (London)* **464**, 176 (2010).
 - [7] M. Boninsegni and N. V. Prokof'ev, *Rev. Mod. Phys.* **84**, 759 (2012).
 - [8] Z.-K. Lu, Y. Li, D. S. Petrov, and G. V. Shlyapnikov, *Phys. Rev. Lett.* **115**, 075303 (2015).
 - [9] N. Henkel, R. Nath, and T. Pohl, *Phys. Rev. Lett.* **104**, 195302 (2010).
 - [10] F. Cinti, P. Jain, M. Boninsegni, A. Micheli, P. Zoller, and G. Pupillo, *Phys. Rev. Lett.* **105**, 135301 (2010).
 - [11] M. Boninsegni, *J. Low Temp. Phys.* **168**, 137 (2012).
 - [12] J. Léonard, A. Morales, P. Zupancic, T. Esslinger, and T. Donner, *Nature (London)* **543**, 87 (2017).
 - [13] J.-R. Li, J. Lee, W. Huang, S. Burchesky, B. Shteynas, F. Ç. Top, A. O. Jamison, and W. Ketterle, *Nature (London)* **543**, 91 (2017).
 - [14] L. D. Landau, *J. Phys. (Moscow)* **5**, 71 (1941).
 - [15] P. Nozières, *J. Low Temp. Phys.* **137**, 45 (2004).
 - [16] D. H. J. O'Dell, S. Giovanazzi, and G. Kurizki, *Phys. Rev. Lett.* **90**, 110402 (2003).
 - [17] L. Santos, G. V. Shlyapnikov, and M. Lewenstein, *Phys. Rev. Lett.* **90**, 250403 (2003).
 - [18] L. Chomaz, R. M. W. van Bijnen, D. Petter, G. Faraoni, S. Baier, J. H. Becher, M. J. Mark, F. Wächtler, L. Santos, and F. Ferlaino, *Nat. Phys.* **14**, 442 (2018).

- [19] D. Petter, G. Natale, R. M. W. van Bijnen, A. Patscheider, M. J. Mark, L. Chomaz, and F. Ferlaino, [arXiv:1811.12115 \(2018\)](#).
- [20] H. Kadau, M. Schmitt, M. Wenzel, C. Wink, T. Maier, I. Ferrier-Barbut, and T. Pfau, *Nature (London)* **530**, 194 (2016).
- [21] I. Ferrier-Barbut, H. Kadau, M. Schmitt, M. Wenzel, and T. Pfau, *Phys. Rev. Lett.* **116**, 215301 (2016).
- [22] L. Chomaz, S. Baier, D. Petter, M. J. Mark, F. Wächtler, L. Santos, and F. Ferlaino, *Phys. Rev. X* **6**, 041039 (2016).
- [23] F. Wächtler and L. Santos, *Phys. Rev. A* **93**, 061603 (2016).
- [24] F. Wächtler and L. Santos, *Phys. Rev. A* **94**, 043618 (2016).
- [25] M. Schmitt, M. Wenzel, F. Böttcher, I. Ferrier-Barbut, and T. Pfau, *Nature (London)* **539**, 259 (2016).
- [26] I. Ferrier-Barbut, M. Wenzel, M. Schmitt, F. Böttcher, and T. Pfau, *Phys. Rev. A* **97**, 011604 (2018).
- [27] R. N. Bisset, R. M. Wilson, D. Baillie, and P. B. Blakie, *Phys. Rev. A* **94**, 033619 (2016).
- [28] M. Wenzel, F. Böttcher, T. Langen, I. Ferrier-Barbut, and T. Pfau, *Phys. Rev. A* **96**, 053630 (2017).
- [29] D. Baillie and P. B. Blakie, *Phys. Rev. Lett.* **121**, 195301 (2018).
- [30] D. Petrov, *Phys. Rev. Lett.* **115**, 155302 (2015).
- [31] C. R. Cabrera, L. Tanzi, J. Sanz, B. Naylor, P. Thomas, P. Cheiney, and L. Tarruell, *Science* **359**, 301 (2018).
- [32] G. Semeghini, G. Ferioli, L. Masi, C. Mazzinghi, L. Wolswijk, F. Minardi, M. Modugno, G. Modugno, M. Inguscio, and M. Fattori, *Phys. Rev. Lett.* **120**, 235301 (2018).
- [33] P. Cheiney, C. Cabrera, J. Sanz, B. Naylor, L. Tanzi, and L. Tarruell, *Phys. Rev. Lett.* **120**, 135301 (2018).
- [34] S. M. Rocuzzo and F. Ancilotto, [arXiv:1810.12229 \(2018\)](#).
- [35] L. Tanzi, E. Lucioni, F. Fama, J. Catani, A. Fioretti, C. Gabbanini, R. N. Bisset, L. Santos, and G. Modugno, [arXiv:1811.02613 \(2018\)](#).
- [36] F. Böttcher, J.-N. Schmidt, M. Wenzel, J. Hertkorn, M. Guo, T. Langen, and T. Pfau, [arXiv:1901.07982 \(2019\)](#).
- [37] K. Aikawa, A. Frisch, M. Mark, S. Baier, A. Rietzler, R. Grimm, and F. Ferlaino, *Phys. Rev. Lett.* **108**, 210401 (2012).
- [38] A. Trautmann, P. Ilzhöfer, G. Durastante, C. Politi, M. Sohmen, M. J. Mark, and F. Ferlaino, *Phys. Rev. Lett.* **121**, 213601 (2018).
- [39] S. Baier, M. J. Mark, D. Petter, K. Aikawa, L. Chomaz, Z. Cai, M. Baranov, P. Zoller, and F. Ferlaino, *Science* **352**, 201 (2016).
- [40] See Supplemental Material at [URL] for details on the experimental setup, measurement schemes, analysis and theory calculations.
- [41] I. Ferrier-Barbut, M. Wenzel, F. Böttcher, T. Langen, M. Isoard, S. Stringari, and T. Pfau, *Phys. Rev. Lett.* **120**, 160402 (2018).
- [42] A. Gammal, T. Frederico, L. Tomio, and P. Chomaz, *J. Phys. B* **33**, 4053 (2000).
- [43] A. Bulgac, *Phys. Rev. Lett.* **89**, 050402 (2002).
- [44] D. S. Petrov, *Phys. Rev. Lett.* **115**, 155302 (2015).
- [45] F. Wächtler and L. Santos, *Phys. Rev. A* **94**, 043618 (2016).
- [46] M. Wenzel, F. Böttcher, J.-N. Schmidt, M. Eisenmann, T. Langen, T. Pfau, and I. Ferrier-Barbut, *Phys. Rev. Lett.* **121**, 030401 (2018).
- [47] B. Josephson, *Phys. Lett.* **1**, 251 (1962).
- [48] J. Javanainen, *Phys. Rev. Lett.* **57**, 3164 (1986).
- [49] S. Raghavan, A. Smerzi, S. Fantoni, and S. R. Shenoy, *Phys. Rev. A* **59**, 620 (1999).
- [50] A similar behavior is also seen for ^{164}Dy for $N < 4000$ (out of the scale of Fig. 1(g)). (.)
- [51] We note that a similar behavior is also found in our ^{166}Er phase diagram but for larger N than the one reported here. (.)
- [52] Y. Tang, A. Sykes, N. Q. Burdick, J. L. Bohn, and B. L. Lev, *Phys. Rev. A* **92**, 022703 (2015).
- [53] M. Greiner, O. Mandel, T. Esslinger, T. W. Hänsch, and I. Bloch, *Nature (London)* **415**, 39 (2002).
- [54] M. Greiner, I. Bloch, O. Mandel, T. W. Hänsch, and T. Esslinger, *Phys. Rev. Lett.* **87**, 160405 (2001).
- [55] B. Paredes, A. Widera, V. Murg, O. Mandel, S. Fölling, I. Cirac, G. V. Shlyapnikov, T. W. Hänsch, and I. Bloch, *Nature (London)* **429**, 277 (2004).
- [56] Z. Hadzibabic, S. Stock, B. Battelier, V. Bretin, and J. Dalibard, *Phys. Rev. Lett.* **93**, 180403 (2004).
- [57] In our absorption imaging a residual asymmetry can be observed between $\pm k_y$. This asymmetry, providing a sharper peak at $k_y > 0$ stems from optical aberrations in our imperfect optical setup. These imperfections make the quantitative analysis of our data more challenging, yet they do not affect the quantitative interpretation. In particular we have checked that the peak structures are also observable along a distinct imaging axis, non-orthogonal to y , using an independent imaging setup. (.)
- [58] M. Takeda, H. Ina, and S. Kobayashi, *J. Opt. Soc. Am.* **72**, 156 (1982).
- [59] C. Kohstall, S. Riedl, E. R. S. Guajardo, L. A. Sidorenkov, J. H. Denschlag, and R. Grimm, *New J. Phys.* **13**, 065027 (2011).
- [60] L. Chomaz, L. Corman, T. Bienaimé, R. Desbuquois, C. Weitenberg, S. Nascimbène, J. Beugnon, and J. Dalibard, *Nat. Commun.* **6**, 6162 (2015).
- [61] S. Hofferberth, I. Lesanovsky, B. Fischer, T. Schumm, and J. Schmiedmayer, *Nature (London)* **449**, 324 (2007).
- [62] The values of a_s^* extracted from experiments and from theory disagree by $4.4 a_0$. Such a mismatch is similar to the one observed in our previous work on the roton instability [18, 19]. This behavior might be related to the possibility that beyond-mean-field effects are not properly accounted by the conventional LHY correction term, see main text. In addition, other effects, such as the dynamics and the atom losses [40], can affect the experimental observations. (.)
- [63] This atom number corresponds to the condensed atom number measured within the stabilization time of a_s [40]. (.)
- [64] M. E. Fisher and A. E. Ferdinand, *Phys. Rev. Lett.* **19**, 169 (1967).
- [65] Y. Imry and D. Bergman, *Phys. Rev. A* **3**, 1416 (1971).
- [66] Y. Imry, *Phys. Rev. B* **21**, 2042 (1980).
- [67] See the theoretical analysis in the revised version of Ref. [35]. (.)
- [68] V. W. Scarola, E. Demler, and S. Das Sarma, *Phys. Rev. A* **73**, 051601 (2006).
- [69] Z.-K. Lu, Y. Li, D. S. Petrov, and G. V. Shlyapnikov, *Phys. Rev. Lett.* **115**, 075303 (2015).
- [70] F. Cinti and M. Boninsegni, *Phys. Rev. A* **96**, 013627

- (2017).
- [71] Y. Kora and M. Boninsegni, [arXiv:1902.08256](#) (2019).
- [72] S. Ronen, D. C. E. Bortolotti, and J. L. Bohn, *Phys. Rev. A* **74**, 013623 (2006).
- [73] A. R. P. Lima and A. Pelster, *Phys. Rev. A* **84**, 041604 (2011).
- [74] A. R. P. Lima and A. Pelster, *Phys. Rev. A* **86**, 063609 (2012).
- [75] V. Cikojevi, L. V. Marki, G. E. Astrakharchik, and J. Boronat, [arXiv:1811.04436](#) (2018).
- [76] A. Barone and G. Paterni, *Physics and applications of the Josephson effect* (Wiley, New York, NY, 1982).
- [77] We note that we have also checked our analysis without performing the recentering step and the same features remain. For instance, for our test data of Fig. 2, the effect being mainly that the side peaks in (e) are more washed out and a slight difference occurs between n_M and n_Φ , both showing still side peaks. ().
- [78] P. Ilzhöfer, G. Durastante, A. Patscheider, A. Trautmann, M. J. Mark, and F. Ferlaino, *Phys. Rev. A* **97**, 023633 (2018).

Supplemental Material

GROUND STATE CALCULATIONS

We perform numerical calculations of the ground state following the procedure detailed in the supplementary information of Ref. [18]. The calculations are based on the conjugate-gradients technique to minimize the energy functional of an eGPE [72]. In particular, the eGPE accounts for the effect of quantum fluctuations, by including the LHY term $\Delta\mu[n] = 32g(na_s)^{3/2}(1 + 3\epsilon_{\text{3d}}^2/2)/3\sqrt{\pi}$ in the system's Hamiltonian (here $g = 4\pi\hbar^2 a_s/m$ and $n = |\psi|^2$ is the spatial density of the macroscopic state ψ). $\Delta\mu[n]$ has been obtained under a local density approximation in Refs. [73, 74]. The relevance of the LHY correction has been demonstrated in various studies of dipolar Bose gases close to the mean-field instability [18, 22–25, 27] as it brings an additional repulsive potential, stabilizing the gas against mean-field collapse at large density. We note that the exact functional form of the potential, originating from beyond mean-field effects, has been questioned by several experimental results in finite-size trapped systems [18, 25, 31, 41], calling for further theory developments [75].

Our numerical calculations provide us with the three-dimensional ground-state wavefunctions $\psi(\mathbf{r})$. From this, we compute the axial in-situ density profile along the trap's weak axis, $n(y) = \int |\psi(\mathbf{r})|^2 dx dz$ and find density profiles, corresponding to the BEC, the supersolid or the ID phase, that we plot in Fig. 1. From the density profiles that exhibit a density modulation, we evaluate S by performing Gaussian fits to each droplet, i.e. to $n(y)$ with y ranging between two neighboring local density minima. From these Gaussian fits, we evaluate the sets of centers $\{y_i^{(0)}\}_i$ and widths $\{\sigma_i\}_i$ cor-

responding to the macroscopic Gaussian wavefunctions $\{\psi_i\}_i$ associated to the individual droplets in the array. We then approximate the droplet wavefunction via $\psi_i(y) \approx \sqrt{n(y \approx y_i^{(0)})} = \alpha_i \exp\left(-\frac{(y - y_i^{(0)})^2}{2\sigma_i^2}\right)$ with α_i a normalization coefficient such that $\int |\psi_i(y)|^2 dy = 1$. We then evaluate the wavefunction overlap S_i between the neighboring droplets $i - 1$ and i via:

$$S_i \equiv \int \psi_{i-1}^*(y) \psi_i(y) dy \quad (1)$$

$$= \sqrt{\frac{2\sigma_i\sigma_{i-1}}{\sigma_i^2 + \sigma_{i-1}^2}} \exp\left(-\frac{(y_i^{(0)} - y_{i-1}^{(0)})^2}{2(\sigma_i^2 + \sigma_{i-1}^2)}\right). \quad (2)$$

The latter equation is obtained via an analytical evaluation of the Gaussian integral. The characteristic link strength defined in the paper is then computed by averaging S_i over all droplet links in the array: $S = \langle S_i \rangle_i$. In our calculation, we only consider as droplets all density peaks of at least 10% of the global density maximum.

LINK STRENGTH AND ESTIMATE OF TUNNELING RATE

Generally speaking, the wavefunction overlap between neighboring droplets relates to a tunneling term, which sets a particle exchange term between two neighboring droplets [47–49, 76]. Following the work of Ref. [46], we perform a first estimate of the tunneling coefficient by simply considering the single-particle part of the Hamiltonian and evaluate it between two neighboring droplets. We note that, in our particular setting where the density modulation is not externally imposed but arises from the mere interparticle interactions, the inter-droplet interaction may also play a crucial role. To perform a more precise estimation of the tunneling between droplets, one would certainly need to properly account for this effect. Here, we stress that our approach simply gives a rough idea of the magnitude of tunneling while it does not aim to be a quantitative description of it. This consideration calls for further studies making a systematic analysis of the full Hamiltonian and of the full phase diagram within the Josephson junction formalism and beyond.

Generalizing the description of Ref. [46] to neighboring droplets of different sizes and amplitudes, which are described by a three-dimensional wavefunction $\psi_i(\mathbf{r})$ approximated to a three-dimensional Gaussian of widths $(\sigma_{i,x}, \sigma_{i,y}, \sigma_{i,z})$ with $\sigma_{i,y} = \sigma_i$, our estimate writes:

$$J_i = \frac{\hbar^2 S_i}{2m} \left[\sum_{k=x,y,z} \frac{1 + \left(\frac{\sigma_{i,k}\sigma_{i-1,k}}{\ell_k^2}\right)^2}{\sigma_{i,k}^2 + \sigma_{i-1,k}^2} + \frac{(y_i^{(0)} - y_{i-1}^{(0)})^2}{2\sigma_i\sigma_{i-1}} \frac{(\sigma_i\sigma_{i-1}/\ell_y)^4 - 1}{\sigma_i^2 + \sigma_{i-1}^2} \right], \quad (3)$$

where $\ell_{x,y,z} = \sqrt{\hbar/m\omega_{x,y,z}}$ are the harmonic oscillator lengths.

In general, the tunnelling coefficients set two typical rates relevant for equilibration processes. The first one is the bare single-particle tunneling rate, which is equal to J_i/h , while the second accounts for the bosonic enhancement from the occupation of the droplet modes and writes $\tilde{t}_i = \sqrt{N_i N_{i-1}} |J_i|/h$ where N_i is the number of atoms in droplet i . In our analysis, we then define the average rates over the droplet arrays as characteristic rates $J/h = \langle J_i \rangle_i/h$, and $\tilde{t} = \langle \tilde{t}_i \rangle_i$; see e.g. [56]. While the ground state evolves from a BEC to a supersolid to an ID, the relevant timescale for achieving (global) equilibrium crosses from being set by the trap frequencies to the above-mentioned tunneling rates.

Using our approximate model, we here give a first estimate of the rates J/h and \tilde{t} as a function of a_s , for the parameters of Fig. 1(b-d) of the main text (i.e. Er quantum gas with $N = 5 \times 10^4$ atoms). Here we find that, for $a_s = a_s^*$, $J/h \sim 400$ Hz and $\tilde{t} \sim 10$ MHz while for $a_s = a_s^* - 2.5 a_0$, $J/h \sim 10^{-7}$ Hz and $\tilde{t} \sim 10^{-3}$ Hz.

TOY MODEL FOR THE INTERFERENCE PATTERN

As described in the main text we use a simple toy model, adapted from Ref. [56], to identify the main features of the TOF interference patterns obtained from an insitu density-modulated state. As a quick reminder, our model considers a one-dimensional array of N_D Gaussian droplets, described by a single classical field, ψ_i , thus neglecting quantum and thermal fluctuations. We compute the TOF density distribution from the free-expansion of the individual ψ_i during a time t via $n(y, t) = |\sum_i \psi_i(y, t)|^2$. In our calculations, we also account for the finite imaging resolution by convolving the resulting $n(y, t)$ with a gaussian function of width σ_{im} . Here we allow the characteristics of the individual ψ_i to fluctuate. In this aim, we introduce noise on the corresponding parameter with a normal distribution around its expectation value and with a variable standard deviation (only ϕ_i can also have a uniform distribution). We then perform a Monte-Carlo study and perform ensemble averages, similar to our experimental analysis procedure. We note that, in this simple implementation, the noise on the different parameters – droplet amplitudes, widths and distances – are uncorrelated.

In the main text, we present results for a single set of parameters, namely $N_D = 4$, $d \equiv \langle d_i \rangle_i = 2.8 \mu\text{m}$ (mean droplet distance), $\sigma_y \equiv \langle \sigma_i \rangle_i = 0.56 \mu\text{m}$ (mean droplet size), $t = 30$ ms, and $\sigma_{\text{im}} = 3 \mu\text{m}$, typical for our experimental Er setting and the corresponding theory expectations in the supersolid regime. $\langle \cdot \rangle_i$ denotes the average over the droplets. In this section, we have a deeper look at the impact of the different parameters on both the

TOF signal and our FT analysis. We study both the fully phase coherent and fully incoherent case, and the unchanged parameters are set as in Fig. 2(j,m) and (l,o).

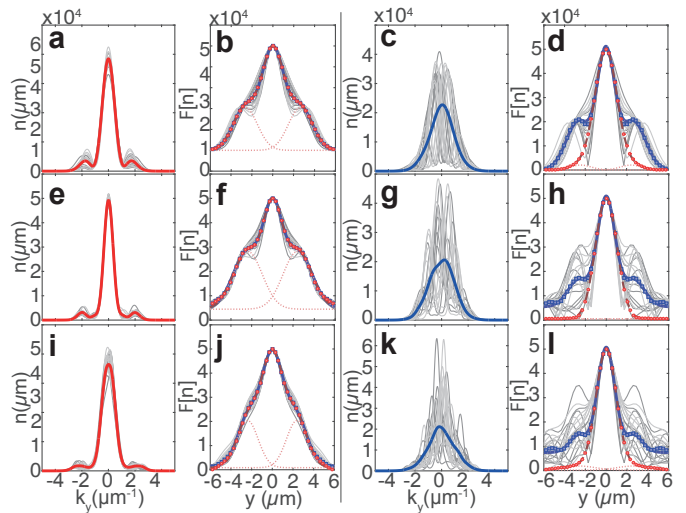


FIG. S1. **Toy model realizations with varying number of droplets N_D .** We use 100 independent draws, and expectation values $d = 2.85 \mu\text{m}$, $\sigma_y = 0.56 \mu\text{m}$ (with 10% noise) and either $\phi_i = 0$ (a,b,e,f,i,j), or ϕ_i uniformly distributed between 0 and 2π (c,d,g,h,k,l). (a–d) $N_D = 2$, (e–h) $N_D = 3$ and (i–l) $N_D = 8$. (a,c,e,g,i,k) TOF density profiles and (b,d,f,h,j,l) corresponding FT analysis of the interference patterns, same color code as Fig. 2.

In Fig. S1, we first exemplify the TOF and FT profiles for a varying number of droplets, between 2 and 8, which cover the range of relevant N_D over the phase diagram of Fig. 1. The results remain remarkably similar to the realization of Fig. 2 with only slight quantitative changes. The main difference lies in the individual interference patterns obtained in the phase incoherent case. With increasing N_D , those profiles become more complex and made of a larger number of peaks (see (c,g,k)). Yet, in this incoherent case, a similar (non-modulated) profile is recovered in the averaged $n(k_y)$ for all N_D . Additionally, we note that for the coherent case with $N_D = 8$, the side peaks in the FT analysis (see (j)) become less visible. By performing additional tests, we attribute this behavior to the limited TOF duration, t , used in our experiment yielding a typical length scale, $\sqrt{\hbar t/m}$ ($= 3.4 \mu\text{m}$), which becomes small compared to the system size ($\approx (N_D - 1)d + \sigma_y$) for large N_D . This intermediate regime in the TOF expansion leads to more complex features, including smaller-sized motifs, in the interference patterns. Finally, when accounting for our imaging resolution, it yields a broadening of the structure observed in the TOF images and less visible peaks in the FT (see (i)). We note that our experiments, because of limited N and additional losses, should rather lie in the regime $2 \leq N_D \leq 5$; see Fig. 1(b).

We then investigate the evolution of the interference

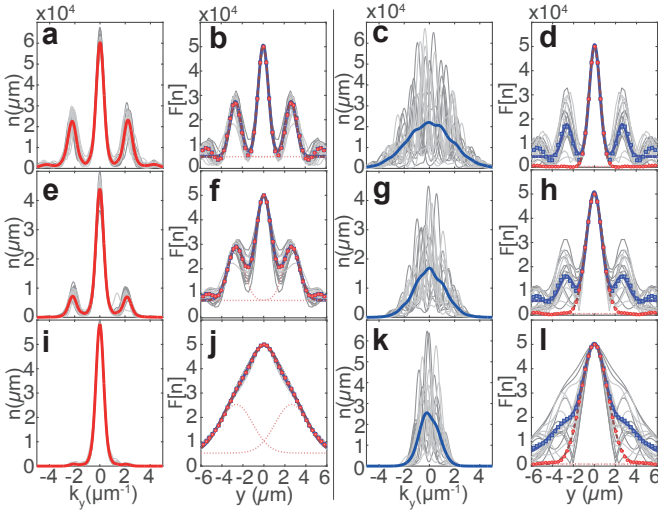


FIG. S2. **Toy model realizations with varying σ_y/d .** We use 100 independent draws, with $N_D = 4$, $d = 2.85 \mu\text{m}$ (with 10% noise) and either $\phi_i = 0$ (a,b,e,f,i,j), or ϕ_i uniformly distributed between 0 and 2π (c,d,g,h,k,l). For each realization we also compute the associated mean S . (a–d) $\sigma_y/d = 0.1$, yielding $S = 1.8 \times 10^{-7}$ (e–h) $\sigma_y/d = 0.15$, matching $S = 1.7 \times 10^{-4}$ and (i–l) $\sigma_y/d = 0.25$, matching $S = 0.028$. (a,c,e,g,i,k) TOF density profiles and (b,d,f,h,j,l) Corresponding FT analysis of the interference patterns, same color code as Fig. 2.

patterns and their FT analysis for a varying mean droplet size, σ_y , while keeping their mean distance, d , fixed. This study is particularly relevant recalling that, within the Josephson junction formalism (see main text and corresponding section of this Supplemental Material), the key parameter controlling the tunneling rate between the droplets is set by the ratio σ_y/d , and the link strength parameter that we use to characterize the supersolid regime scales roughly as $\exp(-(d/2\sigma_y)^2)$. Thus, in our experiment, σ_y/d is intrinsically expected to decrease with the scattering length (see Fig. 3). Performing a direct estimate of the average droplet link from the initial state of our toy model, we find $S = 0.004$ for the calculations of Fig. 2(j–o), lying in an expected supersolid regime yet rather close to the supersolid-to-ID transition. Figure S2 investigates the effect of smaller and larger values of σ_y/d (and consequently of S) on the TOF and FT profiles while independently assuming phase coherence or incoherence. Qualitatively, the features remain similar as in Fig. 2(j–o). In the coherent case, side peaks are visible in the individual as well as in the mean $n(k_y)$ (see (a,e,i)) and yield side peaks in the FT profiles, with $n_{\mathcal{M}} \approx n$ (see (b,f,j)). Increasing (decreasing) σ/d mainly results in a stronger (weaker) signal both in the interference pattern and their FT analysis. Within our toy model, we find that, already for $\sigma/d = 0.25$, the signal nearly vanishes; see (i,j). Even if, given the approximations used in our toy model, this exact value may not fully hold for our

experimental conditions, we expect a similar trend. It is interesting to keep in mind that this effect may limit our capacity of detecting an underlying supersolid state via matter-wave interference in experiments. In the incoherent case, the effect of decreasing σ_y/d mainly results in a broader shape of the mean density profile, while it remains non-modulated; see (c,g,k). In the FT analysis $n_{\mathcal{M}}$ remains structure-less independently of σ_y/d while the structures in $n_{\mathcal{M}}$ becomes sharper with decreasing σ_y/d , as in the coherent case; see (d,h,l).

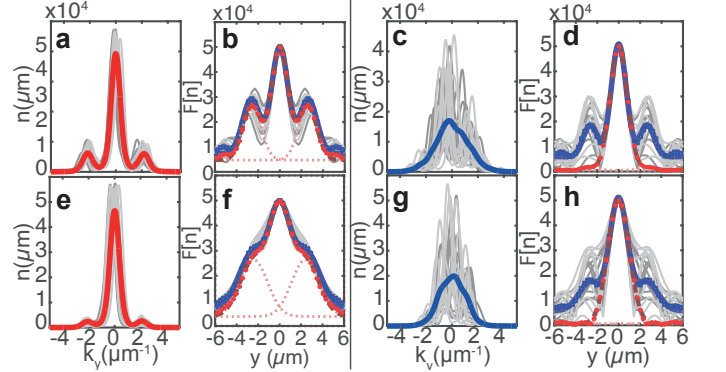


FIG. S3. **Toy model realizations allowing noise in the center position.** We use 100 independent draws, with $N_D = 4$, $d = 2.85 \mu\text{m}$ (with 10% noise), $\sigma_y/d = 0.15$ (a–d) or $\sigma_y/d = 0.2$ (e–h), and either $\phi_i = 0$ (a,b,e,f,i,j), or ϕ_i uniformly distributed between 0 and 2π (c,d,g,h,k,l). Center fluctuation are introduced as normal noise around 0 with standard deviation of $2 \mu\text{m}^{-1}$ in situ (a,c,e,g,i,k) TOF density profiles and (b,d,f,h,j,l) corresponding FT analysis of the interference patterns, same color code as Fig. 2.

Finally, we investigate how a possible shot-to-shot noise on the position of the central interference peak could affect our observables of the density modulation and phase coherence. In the experiments, such fluctuations may occur, for instance, because of beam-pointing fluctuations or excitations of the gas. Although we compensate for such effects by recentering the individual images (see Imaging Analysis section), residual effects may remain, in particular due to center misestimation in the mere presence of the interference patterns of interest. To investigate this aspect, we repeat our toy model calculations now including noise in the global droplet array position and using a standard deviation of $2 \mu\text{m}$ for two values of σ_y/d ; see Fig. S3. Again, qualitatively the observed features remains similar to our prediction in the main text. The main effect lies in the appearance of a small discrepancy in the coherent case between $n_{\mathcal{M}}$ and $n_{\mathcal{M}}$, while the structure in the incoherent case remains similar. As the center misestimation should be the most severe in the latter case (due to the variability of the interference patterns observed here), our test shows the robustness of our analysis procedure against this issue.

IMAGING ANALYSIS: ^{164}Dy AND ^{166}Er

The density distributions in momentum space are extracted from the TOF images using the free-expansion expectation. In the Dy case, the thermal component is subtracted from the individual distribution by cutting out the central region of the cloud and performing an isotropic Gaussian fit on the outer region. This subtraction is beneficial because of the large thermal fraction. In the ^{166}Er case, such a subtraction is on the contrary complicated because of the weak thermal component and this pre-treatment may lead to improper estimation of $A_{\mathcal{M}}$ and A_{Φ} in the later analysis. The obtained momentum density distributions are then recentered and integrated numerically along $k_z(k_x)$ between $[-2.0, +2.0] \mu\text{m}^{-1}$ ($[-1.28, +1.28] \mu\text{m}^{-1}$) to obtain $n(k_y)$ ($n(k_y)$) for ^{164}Dy (^{166}Er). The recentering procedure uses the result a single Gauss fit to the TOF images. The fit is performed after convoluting each image with a Gaussian function of width $0.5 \mu\text{m}$ whose purpose is to reduce the impact of the interference pattern on the center estimation [77].

In order to characterise the system's state, we use the Fourier transform, $\mathcal{F}[n](y)$ of the single density profile, $n(k_y)$. We then compute two average profiles, $n_{\mathcal{M}}$ and n_{Φ} , relying on ensemble average over all measurements under the same experimental conditions; see below for a detailed discussion on $n_{\mathcal{M}}$ and n_{Φ} . In all the measurements reported in this work we use averages over typically 15 to 100 realizations.

To quantify both the existence of a density modulation and global phase coherence on top of this modulation, we fit both $n_{\mathcal{M}}(y)$ and $n_{\Phi}(y)$ with a triple-Gaussian function, where one Gaussian accounts for the central peak and the other Gaussians are accounting for the symmetric side peaks. The amplitudes of the latter give $A_{\mathcal{M}}$ and A_{Φ} , respectively. The distance between the side peaks and the central one is allowed to vary between $[2.5, 2.7] \mu\text{m}$ ($[2.3, 2.5] \mu\text{m}$) in the case of ^{164}Dy (^{166}Er).

DETAILS ON THE FOURIER ANALYSIS

In our analysis we rely on two averaged profiles, named $n_{\mathcal{M}}$ or n_{Φ} , to quantify both the density modulation and its phase coherence. Here we detail the meaning of the average performed.

The Fourier transform (FT) of the integrated momentum distributions, $n(k_y)$, which reads $\mathcal{F}[n](y) = |\mathcal{F}[n](y)| \exp(i \arg(\mathcal{F}[n](y)))$ sets the ground for our analysis. As stated in the main text, an in-situ density modulation of wavelength y^* yields patterns in $n(k_y)$ and consequently induce peaks at $y \approx y^*$, in the FT norm, $|\mathcal{F}[n](y)|$, see Fig. 2(g-i) and (m-o). Spatial variations of the phase relation within the above-mentioned density modulation translate into phase shifts of the interference

patterns, which are stored in the FT argument at $y \approx y^*$, $\arg(\mathcal{F}[n](y^*))$; see also Ref. [56, 61].

The first average that we use is $n_{\mathcal{M}}(y) = \langle |\mathcal{F}[n](y)| \rangle$, i. e. the average of the FT norm of the individual images. As the phase information contained in $\arg(\mathcal{F}[n](y))$ is discarded from $n_{\mathcal{M}}$ when taking the norm, the peaks in $n_{\mathcal{M}}$ probe the mere existence of an insitu density modulation of roughly constant spacing within the different realizations. The second average of interest is $n_{\Phi}(y) = \langle \mathcal{F}[n](y) \rangle$, i. e. the average of the full FT of the individual images. In contrast to $n_{\mathcal{M}}$, n_{Φ} keeps the phase information of the individual realizations contained in $\arg(\mathcal{F}[n](y^*))$. Consequently, peaks in n_{Φ} indicate that the phase relation is maintained over the density modulation, in a similar way for all realizations. Their presence thus provides information on the global phase coherence of a density-modulated state.

EXPERIMENTAL SEQUENCE: ^{164}Dy AND ^{166}Er

$^{166}\text{Erbium}$ - The BEC of ^{166}Er is prepared similarly to Refs. [18, 19, 22, 37]. We start from a magneto-optical trap with 2.4×10^7 ^{166}Er atoms at a temperature of $10 \mu\text{K}$, spin-polarized in the lowest Zeeman sub-level. In a next step we load about 3×10^6 atoms into a crossed optical dipole trap (ODT) operated at 1064 nm . We evaporatively cool the atomic cloud by reducing the power and then increasing the ellipticity of one of the ODT beams. During the whole evaporation a constant magnetic field of $B = 1.9 \text{ G}$ ($a_s = 80 a_0$) along z is applied. We typically achieve BEC with 1.4×10^5 atoms and a condensed fraction of 70%. In a next step the ODT is reshaped in 300 ms into the final trapping frequencies $\omega_{x,y,z} = 2\pi \times (145, 31.5, 151) \text{ Hz}$. Consecutively, we ramp B linearly to 0.62 G ($64.5 a_0$) in 50 ms and obtain a BEC with 8.5×10^4 atoms, which are surrounded by 3.5×10^4 thermal atoms. This point marks the start of the ramp to the final a_s .

$^{164}\text{Dysprosium}$ - For the production of a ^{164}Dy BEC we closely follow the scheme presented in [38]. Starting from a 3 s loading phase of our 5-beam MOT in open-top configuration [78], we overlap a 1064 nm single-beam dipole trap with a $1/e^2$ -waist of about $22 \mu\text{m}$, for 120 ms. Eventually, we transfer typically 8×10^6 atoms utilizing a time averaging potential technique to increase the spatial overlap with the MOT. After an initial 1.1 s evaporative cooling phase by lowering the power of the beam, we add a vertically propagating beam, derived from the same laser, with a $1/e^2$ -waist of about $130 \mu\text{m}$ to form a crossed optical dipole trap for additional confinement. Subsequently, we proceed forced evaporative cooling to reach quantum degeneracy by nearly exponentially decreasing the laser powers in the two dipole-trap beams over 3.6 s. We achieve BECs of ^{164}Dy with typically 10^5 atoms and condensate fractions of about 40%. During

the entire evaporation sequence the magnetic field is kept constant at 2.5 G pointing along the vertical (z -) axis.

To be able to condense directly into the supersolid, we modify the dipole trap to condense at a stronger confinement of $\omega_{x,y,z} = 2\pi \times (225, 37, 134)$ Hz. After a total evaporative cooling duration of 3.1 s, we achieve Bose-Einstein condensation at 2.55 G and reach a state with supersolid properties at 2.43 G, keeping the magnetic field constant throughout the entire evaporation sequence for both cases.

Time of flight and imaging for ^{166}Er and ^{164}Dy - In order to probe the momentum distribution of the Dy (Er) gases, we switch off the confining laser beams and let the atoms expand freely for 18 ms (15 ms), while keeping the magnetic field constant. Consecutively the amplitude of B is increased to a fixed amplitude of 5.4 G (0.6 G). In the case of ^{164}Dy , the magnetic field orientation is rotated in order to point along the imaging axis. This ensures constant imaging conditions for different a_s . After an additional 9 ms (15 ms) we perform a standard absorption imaging.

TUNING THE SCATTERING LENGTH IN ^{166}Er AND ^{164}Dy

$^{166}\text{Erbium}$ - All measurements start with a BEC at $64.5 a_0$. In order to probe the BEC-supersolid-ID region, we linearly ramp a_s to its target value in $t_r = 20$ ms by performing a corresponding ramp in B . Due to a finite time delay of the magnetic field in our experimental setup and the highly precise values of a_s needed for the experiment, we let the magnetic field stabilize for another 15 ms before $t_h = 0$ starts. By this, we ensure that the residual lowering of a_s during the entire hold time is $\lesssim 0.3 a_0$. In the main text, we always give the a_s at $t_h = 0$. Furthermore, we estimate our magnetic field uncertainty to be ± 2.5 mG, leading to a $\pm 0.2 a_0$ uncertainty of a_s in our experiments.

To choose the best ramping scheme, we have performed experiments varying t_r from 0.5 ms to 60 ms, ramping to a fixed a_s lying in the supersolid regime, and holding for $t_h = 5$ ms after a fixed 15 ms waiting time. We record the evolution of A_Φ as a function of t_r ; see Fig. S4. When increasing t_r , we first observe that A_Φ increases, up to $t_r = 20$ ms, and then A_Φ gradually decreases. The initial increase can be due to diabatic effects and larger excitation when fast-crossing the phase transition. On the other hand, the slow decrease at longer t_r can be explained by larger atom loss during the ramp. We then choose $t_r = 20$ ms as an optimum value where a supersolid behavior develops and maintains itself over a significant time while the losses are minimal.

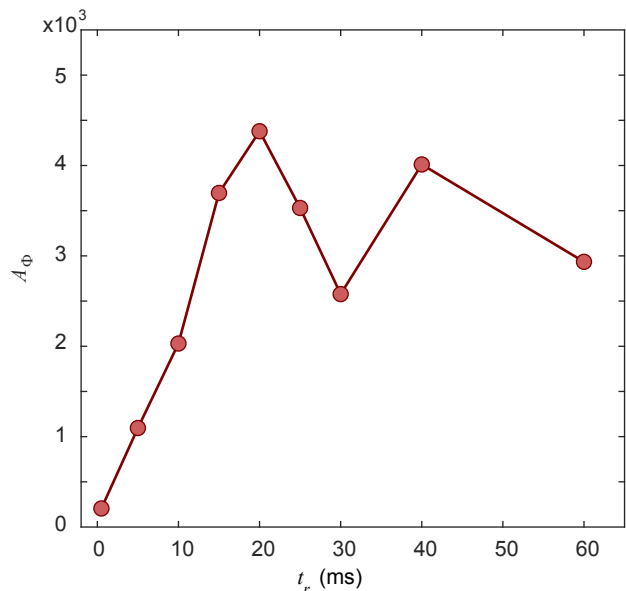


FIG. S4. **Ramp time effect on the supersolid behavior** Measured A_Φ for various durations of the scattering-length ramp with ^{166}Er and a final $a_s = 54.1(2) a_0$. All measurements include a 15 ms stabilization time after t_r and are performed with an additional hold of $t_h = 5$ ms.

$^{164}\text{Dysprosium}$ - As the value of the background scattering, a_{bg} length for ^{164}Dy is still under debate [25, 41, 52], we discuss the experimental settings in terms of magnetic field. Yet, to gain a better understanding of the tunability of a_s in our experiment, we first perform a Feshbach spectroscopy scan on a BEC at $T = 60$ nK. After evaporative cooling at $B = 2.5$ G, we jump to B varying from 1 G to 7.5 G and we hold the sample for 100 ms. Finally, we switch off the trap, let the cloud expand for 26 ms and record the total atom number as a function of B . We then fit the observed loss features with a gaussian fit to obtain the position $B_{0,i}$ and width ΔB_i of the FRs, numbered i . We finally use the standard Feshbach resonance formula to estimate the a_s -to- B dependence via $a_s(B) = a_{\text{bg}} \prod_i (1 - \Delta B_i / (B - B_{0,i}))$. Here we account for 8 FRs located between 1.2 G and 7.2 G. Depending on the background scattering length a_{bg} , the overall magnitude of $a_s(B)$ changes. We can get an estimate of a_{bg} from literature. In Fig. S5, we use the value of a_s from Ref. [52] obtained at 1.58 G close to the B -region investigated in our experiment, $a_s = 92(8) a_0$. By reverting the $a_s(B)$ formula, we set $a_{\text{bg}} = 87(8) a_0$. For the measurements of Figs. 4-5, we ramp B linearly from 2.5 G in 20 ms to a final value ranging from 1.8 to 2.1 G, for which we estimate a_s ranging from $97(9) a_0$ to $105(10) a_0$. We calibrate our magnetic field using RF spectroscopy, with a stability of about 2 mG. In the Dy case, we do not apply an additional stabilization time. This is justified because of the more mellow a_s -to- B dependence in the B -range of interest as well as of the wider a_s -range of the super-

osolid regime (see Fig. 1) compared to the Er case. For the measurements of Figs. 6–7, we use two B -values, namely 2.43 G and 2.55 G, at which we perform the evaporative cooling scheme. Here we estimate $a_s = 109(10) a_0$ and $a_s = 134(12) a_0$, respectively.

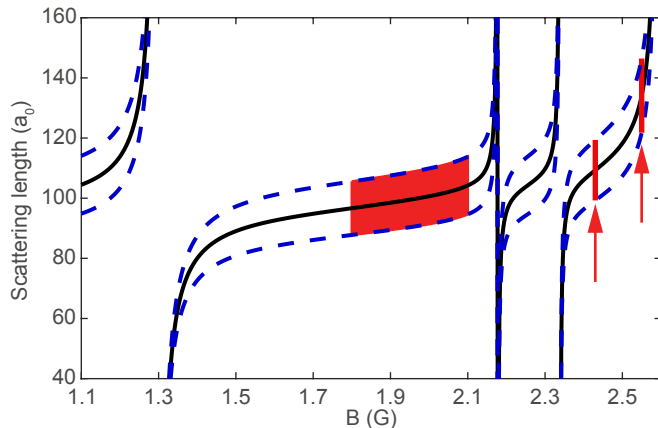


FIG. S5. **Estimated scattering length tuning in ^{164}Dy** Estimated dependence of a_s on B for ^{164}Dy . The FR positions and widths have been extracted from trap-loss spectroscopy measurements, the background scattering length is estimated to $a_{\text{bg}} = 87(8) a_0$, see text. The blue dashed line gives an error-estimate considering only the errorbar on a_{bg} from the mere a_s measurement of Ref. [52] and not accounting for uncertainty of the Feshbach scan. For Figs. 4-5, we use B between 1.8 G and 2.1 G (red area); for Figs. 6-7, we keep at two constant B -values, namely 2.43 G and 2.55 G (red arrows).

ATOM LOSSES IN ^{166}Er AND ^{164}Dy

As pointed out in the main text, in the time evolution of the quantum gases in both the supersolid and the ID regime, inelastic atom losses play a crucial role. The atom losses are increased in the above mentioned regime as (i) higher densities are required so that a stabilization under quantum fluctuation effects becomes relevant and (ii) the magnetic field may need to be tune close to a FR pole to access the relevant regime of interaction parameters. (i) is at play for all magnetic species but more significant for ^{166}Er due to the smaller value of a_{dd} . (ii) is relevant for both ^{166}Er and ^{162}Dy but conveniently avoided for ^{164}Dy thanks to the special short-range properties of this isotope.

To quantify the role of these losses, we report here the evolution of the number of condensed atoms, N , as a function of the hold time in parallel to the phase coherent character of the density modulation observed. We count N by fitting the thermal fraction of each individual image with a two-dimensional Gaussian function. To ensure that only the thermal atoms are fitted, we mask out the central region of the cloud associated with the quantum

gas. Afterwards we subtract this fit from the image and perform a numerical integration of the resulting image (so called pixel count) to obtain N .

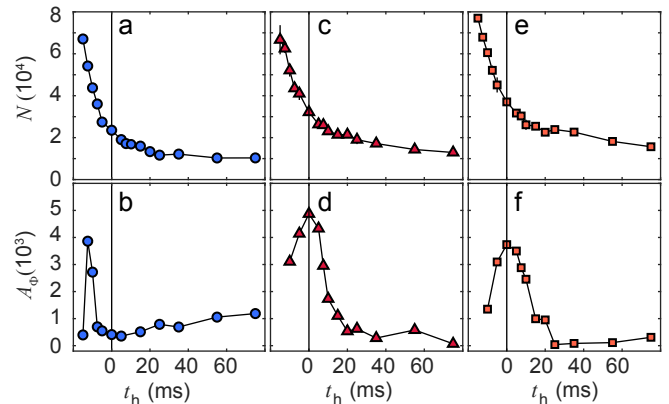


FIG. S6. **atom number and coherence decays in ^{166}Er** Time evolution of N and A_Φ for ^{166}Er at different a_s , including points before $t_h = 0$ ms in the experiment. The corresponding scattering lengths are $53.3(2) a_0$ (a,b), $54.0(2) a_0$ (c,d), $54.2(2) a_0$ (e,f).

$^{166}\text{Erbium}$ - In the Er case, a 15 ms stabilization time is added to ensure that a_s is reached up to $0.3 a_0$. During this time, i. e. for $t_h < 0$, we suspect that the time-evolution of the cloud properties is mainly dictated by the mere evolution of the scattering length. Therefore, in the main text, we report on the time evolution for $t_h \geq 0$. We note that because of the narrow a_s -range for the supersolid regime, the long stabilization time for a_s is crucial. However, because of the significant role of the atom losses in our system, in particular for ^{166}Er , the early evolution of N and the cloud's properties are intimately connected. Therefore, the early time evolution at $t_h < 0$ is certainly of high importance for our observations at $t_h \geq 0$.

To fully report on this behavior, we show the evolution of N and A_Φ during both the stabilization and the holding time in Fig. S6 for three different a_s values – either in the ID (a, b) or supersolid regime (c-f). The time evolution shows significant atom loss, prominent already during the stabilization time, and levels off towards a remaining atom number at longer holding times in which we recover small BECs. Simultaneously, in each case reported here, we observe that during the stabilization time A_Φ increases and a coherent density modulated state grows. This density modulation starts to appear at a typical atom number of $N \gtrsim 6 \times 10^4$ and consecutively decays. For the lower $a_s = 53.3(2) a_0$ case, we observe that the coherent state does not survive the a_s stabilization time, and decays faster than the atoms loss; see Fig. S6 (a, b). This behavior corresponds to the ID case discussed in the main text. The central point of the present work is to identify a parameter range where the coherence of the density modulated state survives for $t_h > 0$ and its decay

TABLE I. Extracted 1/10-lifetime of ^{166}Er atom number decay for $t_h \geq 0$ and remaining atom number at long holding time for data in Fig. S6.

$a_s(a_0)$	t_N (ms)	$N_r(10^4)$	t_Φ (ms)
53.3(2)	32(5)	1.03(5)	-
54.0(2)	51(9)	1.29(11)	25(6)
54.2(2)	46(12)	1.7(2)	32(9)

time scale is similar to the one of the atom loss. In order to quantify a timescale for the atom number decay, we fit an exponential decay to $t_h \geq 0$ ms. Here we allow an offset N_r of the fit, accounting for the BEC recovered at long holding times. In Table I, we report on the typical 1/10-decay times of the atom number, which are up to 50 ms. These values are of the order as the extracted t_Φ , see Table I and Fig. 5 of the main text. This reveals that in ^{166}Er the extracted lifetime of the coherent density modulated states are mainly limited by atom loss.

Furthermore we note that the extracted N_r values for the recovered BECs are smaller than 2×10^4 , which is consistent with the BEC region found in the phase diagram

of Fig. 1(f).

$^{164}\text{Dysprosium}$ - Differently from the ^{166}Er case, for ^{164}Dy , we operate in a magnetic-field range in which the three-body collision coefficients are small and only moderate atom losses occur. This enables the observation of an unprecedented long-lived supersolid behavior. To understand the effects limiting the supersolid lifetime, we study the lifetime of the condensed-atom number for different B . We perform this detailed study for the data of Fig. 5 of the main text, which are obtained after preparing a stable BEC and then ramping B to the target value. Fig. S7 shows the parallel evolution of N and A_Φ for three different magnetic field values 1.8 G, 2.04 G and 2.1 G. Here we observe that, for all B values, A_Φ seems to decay faster than the atom number. This suggests that the lifetime of the density-modulated state in our ^{164}Dy experiment is not limited by atom losses. To confirm this observation, we extract the 1/10 lifetimes of both N and A_Φ ; see Table II. The values confirm our observation and shows an atom number lifetime larger than t_Φ at least by a factor of ≈ 5 . In addition, we find that the ratio t_N/t_Φ varies, indicating that atom losses are not the only mechanism limiting the lifetime of the supersolid properties in Dy.

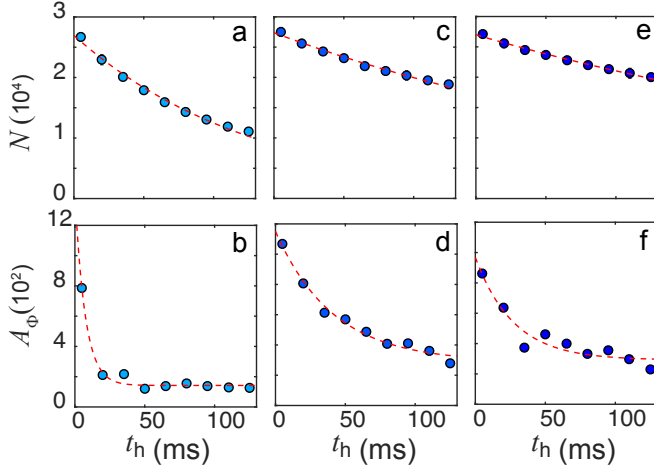


FIG. S7. **atom number and coherence decays in ^{164}Dy** Time evolution of N and A_Φ for ^{164}Dy at different B for the data of Fig. 5. The corresponding magnetic fields are 1.8 G (a,b), 2.04 G (c,d), 2.1 G (e,f).

TABLE II. Extracted 1/10-lifetime of ^{164}Dy atom number decay and A_Φ decay for data in Fig. S7.

B (G)	t_N (ms)	t_Φ (ms)
1.8	300(12)	12(5)
2.04	728(34)	152(13)
2.1	926(36)	133(25)